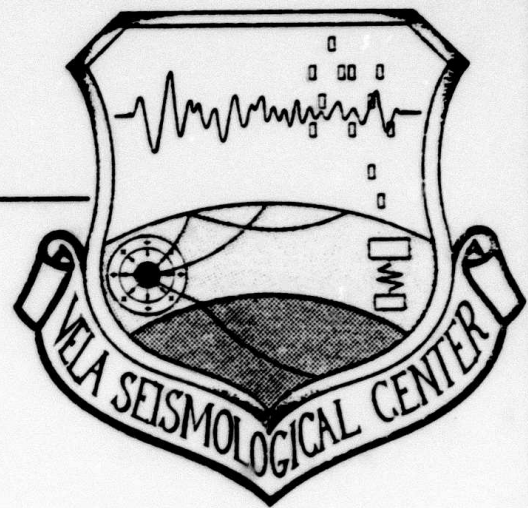


AD A121617

VSC-TR-82-24

THE PHYSICAL BASIS OF $m_b:M_s$
AND VARIABLE FREQUENCY
MAGNITUDE METHODS FOR
EARTHQUAKE/EXPLOSION
DISCRIMINATION



J. L. Stevens
S. M. Day

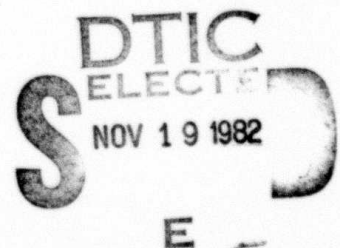
SYSTEMS, SCIENCE AND SOFTWARE
P. O. Box 1620
La Jolla, California 92038

TOPICAL REPORT

June 1982

Approved for Public Release,
Distribution Unlimited

Monitored by:
VELA Seismological Center
312 Montgomery Street
Alexandria, Virginia 22314



DTIC FILE COPY

82 11 19 004

Unclassified

SECURITY CLASSIFICATION OF THIS PAGE (When Data Entered)

REPORT DOCUMENTATION PAGE		READ INSTRUCTIONS BEFORE COMPLETING FORM
1. REPORT NUMBER VSC-TR-82-24	2. GOVT ACCESSION NO. AD-A121617	3. RECIPIENT'S CATALOG NUMBER
4. TITLE (and Subtitle) The Physical Basis of $m_b:M_s$ and Variable Frequency Magnitude Methods for Earthquake/Explosion Discrimination		5. TYPE OF REPORT & PERIOD COVERED Topical Report
6. PERFORMING ORG. REPORT NUMBER SSS-R-82-5595		7. CONTRACT OR GRANT NUMBER F08606-79-C-0008
8. AUTHOR J. L. Stevens S. M. Day		9. PROGRAM ELEMENT PROJECT AREA & WORK UNIT NUMBERS Program Code No. 6H189 APRA Order No. 443E
10. PERFORMING ORGANIZATION NAME AND ADDRESS Systems, Science and Software P.O. Box 1620 La Jolla, California 92038		11. REPORT DATE June 1982
12. CONTROLLING OFFICE NAME AND ADDRESS VELA Seismological Center 312 Montgomery Street Alexandria, Virginia 22314		13. NUMBER OF PAGES 87
14. MONITORING AGENCY NAME & ADDRESS (if different from Controlling Office)		15. SECURITY CLASS. of this report Unclassified
		16. DECLASSIFICATION DOWNGRADING SCHEDULE
17. DISTRIBUTION STATEMENT (of this Report) Approved for Public Release, Distribution Unlimited.		
18. DISTRIBUTION STATEMENT (of the abstract entered in Block 20, if different from Report)		
19. SUPPLEMENTARY NOTES		
20. KEY WORDS (Continue on reverse side if necessary and identify by block number) Discrimination Earthquake/explosion discrimination $m_b:M_s$ VFM Variable Frequency Magnitude Explosion seismology Earthquake modeling		
21. ABSTRACT (Continue on reverse side if necessary and identify by block number) We analyze the theoretical basis for the ($m_b:M_s$) and Variable Frequency Magnitude (VFM) earthquake/explosion discriminants in light of recent results from numerical modeling of earthquake and explosion dynamics. We examine the effects of source mechanism (double-couple versus point dilatation), source depth, source spectra, and source region elastic structure. We use six three-dimensional finite difference simulations of earthquakes for the earthquake source models, and four empirical (Mueller-Murphy) and four numerical models for explosions — (continued)		

DD FORM 1 JAN 73 1473 EDITION OF NOV 68 IS OBSOLETE

Unclassified

SECURITY CLASSIFICATION OF THIS PAGE (When Data Entered)

ABSTRACT: (continued)

in different materials. We estimate that source mechanism (i.e., quadrupole versus monopole) contributes about .35 magnitude on the average to the separation between earthquakes and explosions on a $m_b:M_s$ diagram. Differences in source region elastic properties tend to increase the separation, contributing a factor of approximately $\sqrt{\rho\alpha^3}$ (ρ = density, α = P-wave speed) to the ratio of surface wave amplitude to body wave amplitude. For events with $M_s < 4.0$, this effect may be more important than source spectral differences, especially for explosions in low velocity materials.

VFM discrimination depends primarily on spectral differences between earthquakes and explosions. Theoretical separation of the earthquake and explosion populations is very clear for explosions in granite at frequencies of 2 Hz or greater with $m_b > 4.0$. Smaller events may be discriminated using higher frequencies. Separation is not as good for explosions in low velocity materials such as tuff, especially at low yields.

For small events, the $m_b:M_s$ and VFM discrimination methods work (or fail) for quite different reasons. Interference with pP causes earthquake and explosion populations to converge on the $m_b:M_s$ plane at m_b 4.5 using an empirical depth/yield relation of $d = 122W^{1/3}$ meters. This interference increases the separation using VFM, allowing the method to work even for very low yields. More deeply buried small explosions may be discriminated by $m_b:M_s$, but not by VFM. Simultaneous use of both methods should allow improved discrimination.

AFTAC Project Authorization No. VT/0712/B/PMP
ARPA Order No. 4436, Program Code No. 6H189
Effective Date of Contract: November 17, 1978
Contract Expiration Date: November 15, 1981
Amount of Contract: \$1,816,437
Contract No. F08606-79-C-0008
Principal Investigator and Phone No.
Dr. J. Theodore Cherry, (714) 453-0060
Project Scientist and Phone No.
Mr. Brian W. Barker, (202) 325-7581

This research was supported by the Advanced Research Projects Agency of the Department of Defense and was monitored by AFTAC/VSC, Patrick Air Force Base, Florida 32925, Under Contract No. F08606-79-C-0008.

The views and conclusions contained in this document are those of the authors and should not be interpreted as necessarily representing the official policies, either expressed or implied, of the Advanced Research Projects Agency, the Air Force Technical Applications Center, or the U. S. Government.

W/O 11098



Accession For	
NTIS GRA&I	<input checked="checked" type="checkbox"/>
DTIC TAB	<input type="checkbox"/>
Unannounced	<input type="checkbox"/>
Justification	
By	
Distribution/	
Availability Codes	
Dist	Avail and/or Special
A	

TABLE OF CONTENTS

<u>Section</u>	<u>Page</u>
I. INTRODUCTION.	1
II. SOURCE MODELS	5
2.1 EARTHQUAKE MODELS	5
2.2 EXPLOSION MODELS.	10
III. EFFECT OF SOURCE MECHANISM.	13
IV. EFFECT OF DEPTH	25
V. EFFECT OF SOURCE REGION ELASTIC PROPERTIES.	31
VI. SPECTRAL COMPARISON OF SOURCES.	35
VII. TIME-DOMAIN SOURCE COMPARISON	50
VIII. RECOMMENDATIONS FOR FURTHER RESEARCH.	58
IX. DISCUSSION AND CONCLUSIONS.	61
X. REFERENCES.	65
APPENDIX A: MUELLER-MURPHY EXPLOSION SOURCE FUNCTION AND SCALING LAWS.	70
APPENDIX B: EQUIVALENT JUMP VECTORS FROM UPGOING AND DOWNGOING WAVES	74
APPENDIX C: INTERPOLATION METHOD.	79
APPENDIX D: UPGOING AND DOWNGOING WAVES FOR ARBITRARY FAULT ORIENTATION	83

LIST OF ILLUSTRATIONS

<u>Figures</u>	<u>Page</u>
1. Sketches of six earthquake source models used in this study.	6
2. Far-field displacement spectra, and corresponding wave-forms at two azimuths for the six theoretical earthquake sources used in the study	9
3. Distribution of magnitude differences for several depths and takeoff angles	19
4. Frequency distribution of the difference between earthquake and explosion magnitudes due to source mechanism alone	21
5. Contour plot of frequency distribution in $m_b:M_s$ plane . .	23
6. Spectral amplitude of direct P plus elastic pP with a time delay of 0.5 seconds	26
7. Relative Rayleigh wave amplitudes as a function of frequency, depth and dip angle.	29
8. Moment versus surface wave magnitude.	37
9. $m_b:M_s$ comparison using source spectra at one and twenty seconds.	39
10. Spectral comparison of earthquake sources with a 100 KT explosion in Tuff.	41
11. Spectral comparison of numerical explosion models at 100 KT with earthquake number 1	42
12. Spectral comparison of Mueller-Murphy explosion models at 100 KT with earthquake number 1.	43
13. Spectral comparison of 2.5 KT Mueller-Murphy Tuff explosion with earthquake number 3.	45
14. Synthetic variable frequency magnitude curves using $f_1=0.05$ Hz for the low frequency and $f_2=1.0$ Hz and 2.0 Hz for the high frequency	46
15. Synthetic Variable Frequency Magnitude curves for $f_1=0.5$ Hz, $f_2=2.0, 3.0$, and 4.0 Hz.	47
16. Synthetic Variable Frequency Magnitude curves for $f_1=0.8$ Hz, $f_2=2.0, 3.0$ and 4.0 Hz	48
17. Time-domain m_b measurements from synthetic seismograms of the six earthquake sources scaled to different sizes and Mueller-Murphy explosion sources in salt, tuff, granite, and shale at 10, 100 and 1000 KT	57
18. Fault and global coordinates used for synthetic seismograms	85

LIST OF TABLES

<u>Table</u>		<u>Page</u>
1.	PROPERTIES OF EXPLOSIONS SOURCES.12
2.	RELATIVE AMPLITUDE FACTORS FOR POINT DISLOCATIONS17
3.	SOURCE REGION STRUCTURE FOR SYNTHETICS.51
4.	MAGNITUDE ESTIMATES FROM SYNTHETIC EARTHQUAKE SEISMOGRAMS53
5.	MAGNITUDE ESTIMATES FROM SYNTHETIC EXPLOSION SEISMOGRAMS55
A.	MUELLER/MURPHY EMPIRICAL CONSTANTS73

I. INTRODUCTION

A number of methods have been proposed for discriminating earthquakes from underground nuclear explosions using characteristics of the seismic signal observed at teleseismic and regional distances. The $m_b:M_s$ and Variable Frequency Magnitude (VFM) discriminants, in particular, have received extensive study, and each has a well-established empirical basis. Theoretical understanding of these discriminants, however, is quite incomplete. In view of the prominent role envisioned for seismic methods in detecting and identifying underground nuclear explosions, it is important that these techniques be quantitatively understood on the basis of earthquake and explosion physics. Only with a quantitative model describing why the discriminants work, can we confidently predict the circumstances under which they may fail.

The difference between body wave magnitude, m_b , and surface wave magnitude, M_s , is usually larger for explosions than for earthquakes. The separation between the earthquake and explosion populations on the $m_b:M_s$ plane has been documented in many observational studies. Marshall and Basham (1972), for example, show m_b separation for Eurasian events with a given M_s ranging from about 0.5 to 1.5 m_b units with somewhat better separation for larger-magnitude events than for small ones. Another proposed discriminant, the Variable Frequency Magnitude (VFM) method (Archambeau, Harkrider and Helmberger, 1974) is based on the spectral content of the short-period P-wave. In this method, the body-wave magnitude is measured from narrow-band-filtered seismograms at two different frequencies, f_1 and f_2 . A plot of $m_b(f_1)$ versus $m_b(f_2)$ also produces, in many circumstances, a clear separation of the earthquake and explosion populations (Savino, Archambeau and Masso, 1980).

Although the empirical results are well-known, theoretical understanding of the discriminants has been impeded by lack of adequate models of the earthquake source. Kinematic, semiempirical

models of earthquakes such as the Haskell (1964, 1966), Brune (1970), and Aki (1967, 1972) models have been available, but these models contain free parameters such as the rise time or corner frequency which are difficult to constrain and crucial to the analysis of discrimination methods. Aki, Bouchon and Reasenberg (1974) apply the earthquake spectral theory of Aki to argue that source spectrum (or equivalently, source time history) alone can account for about 1 magnitude unit separation in m_b for events with M_s as low as 2. On the other hand, Douglas, Hudson and Kemphavi (1971), using point sources in a half-space, argue that differences in source mechanism (double-couple versus point dilatation) alone are sufficient to give reasonable discrimination between explosions and earthquakes except for a few preferred orientations of the double-couple. Douglas, Hudson and Blamey (1972), using synthetic seismograms for layered media, and using point and extended earthquake sources, come to the conclusion that source mechanism is most important to discrimination. They also find that explosions in soft materials have a greater separation between m_b and M_s than explosions in harder materials.

Archambeau, Harkrider and Helmberger (1974) first developed the physical basis for the VFM discriminant and explained the differences between m_b and M_s of earthquakes and explosions on the basis of characteristic spectral differences. They also looked at applications of the VFM method to the discrimination of multiple explosions. The earthquake model used in that study was a growing, propagating, transparent spherical cavity (Archambeau, 1968). The explosion model used was an early version of the finite difference models used here. In this study, we reduce uncertainties about the source spectra by using a more appropriate failure geometry with more realistic boundary conditions for our earthquake models, more refined numerical explosion models, and an empirical explosion model which is constrained by near field observations.

Von Seggern and Rivers (1979) evaluated the reliability of a number of earthquake/explosion discriminants, using methods similar to those used in this report, and applied them to events in the

western United States. In general, their conclusions agree with ours; however, there are three important differences. First, our improved source models allow increased confidence in our estimates of spectral differences between earthquakes and explosions. Second, in their estimation of P-wave amplitudes, they use a whole space solution, neglecting the transmission coefficient (Equation (5.2)) which should be included if the earthquake and explosion are in different materials. This transmission coefficient reduces the separation between earthquakes and explosions on the $m_b:M_s$ plane. Finally, their estimate of source mechanism effects was based on root mean square averages of the radiation pattern while we computed distribution functions by directly calculating amplitudes for a large number of orientations.

It is important to understand the relative contribution of source mechanism and source spectrum to m_b and M_s of earthquakes since the two phenomena have very different implications for the applicability of the discriminant at low magnitude. The effect of source mechanism is independent of source size whereas the effect of spectral shape inevitably vanishes below some threshold size. Furthermore, if the observed m_b-M_s of earthquakes is predominantly an effect of source spectrum rather than source mechanism, then the discriminant will be more likely to fail for high stress-drop earthquakes.

Conclusions about the influence of earthquake complexity on $m_b:M_s$ are also highly dependent on the source model. Blandford (1975) suggested that increasing the complexity of an earthquake, by subdividing into many small earthquakes, causes an ever increasing earthquake corner frequency. This would imply that increasing the complexity makes the earthquake more explosion-like.

The purpose of this study is to refine the theoretical basis of the $m_b:M_s$ and VFM methods. Clearly, it is important for this purpose to use an earthquake source model which is analytically sound and relatively free from non-physical assumptions. We will use theoretical source spectra (and time histories) obtained from

three-dimensional numerical simulations of earthquakes by Day (1979, 1982a, 1982b). A range of sources is considered, including uniform stress-drop events, isolated stress concentration events, and multiple-stress-concentration events. We use two types of explosion sources for comparison: the one-dimensional (spherically symmetric) numerical simulations of Cherry, Rimer and Wray (1975), and the empirical explosion source model of Mueller and Murphy (1971).

We first give separate consideration to each of four factors likely to contribute to differences between earthquake and explosion seismograms. These are source mechanism (i.e., double-couple versus center-of-dilatation), source depth, source-region elastic structure, and source spectrum (or time-history). After analyzing these factors separately, we make time-domain m_b estimates using synthetic seismograms which incorporate, simultaneously, effects of free-surface reflection, crustal structure, source mechanism, and source finiteness. We restrict consideration to earthquakes and explosions occurring in the same general area so that travel path and attenuation effects can be considered the same for all sources.

II. SOURCE MODELS

2.1 EARTHQUAKE MODELS

Dynamic earthquake models in the sense used here are those which specify the tectonic prestress and the resisting (frictional) stresses in the source region, and derive the resulting displacement discontinuity (slip) via the equations of motion. Such earthquake models generally lead to nonlinear, mixed boundary value problems requiring numerical methods for their solution. Only recently have three-dimensional solutions for finite faults become available. The dynamic models for which numerical solutions have been obtained fall into two categories: fixed-rupture-velocity models, in which rupture velocity is a specified constant, and spontaneous rupture models, in which rupture velocity is determined by some failure criterion, then derived as part of the numerical solution.

Six of the dynamic earthquake simulations performed by Day (1979, 1982a,b) provide the basis for the earthquake source functions used in this study. Three of these are for fixed-rupture-velocity models and three are for spontaneous rupture models. The former are uniform stress-drop events, while the latter incorporate various forms of non-uniform stress-drop. The physical basis of these simulations, as well as a detailed discussion of the resultant fault slip histories, is given in the above references. Here we only outline the main characteristics of the computed rupture histories and far-field seismic radiation.

The final perimeters of the six fault surfaces are sketched in Figure 1. Models 3, 4, and 5 are fixed-rupture-velocity cases in which the rupture grows circularly outward from the center of the fault at a velocity of 90 percent of the shear wave speed β , and stops abruptly at the prescribed perimeter. Models 1, 2, and 6 are spontaneous rupture cases. For these models, the distribution of prestress on the plane of faulting is as shown in the figure. The dynamic stress-drop, which is the difference between the shear prestress and the sliding frictional stress on the fault, is

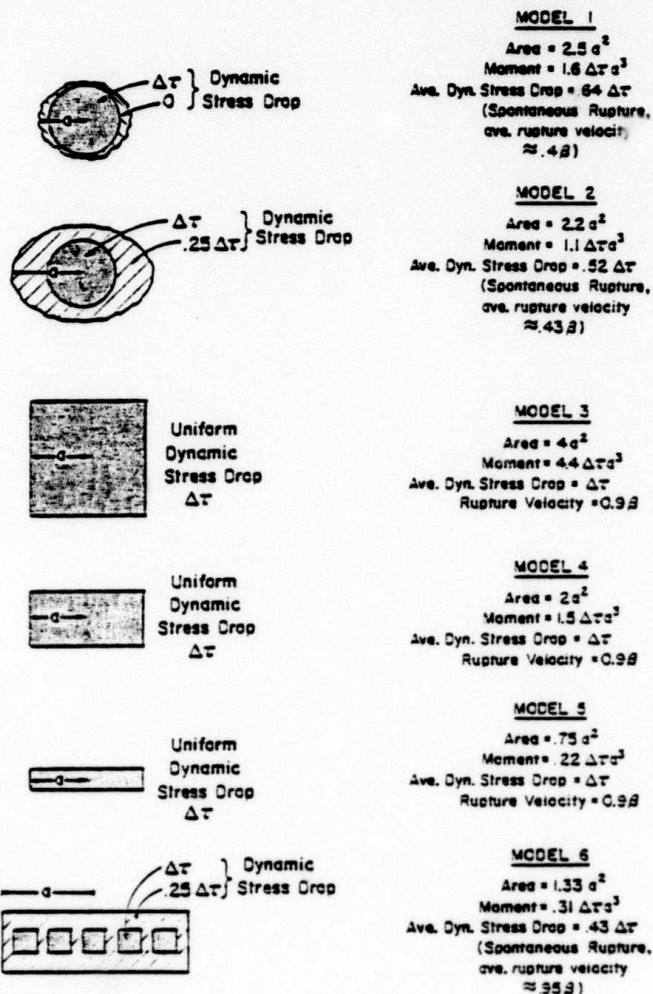


Figure 1. Sketches of six earthquake source models used in this study. The final half-length of the fault is denoted by a , the maximum dynamic stress-drop by $\Delta\tau$. Models 3, 4, and 5 are fixed rupture velocity models and 1, 2, and 6 are spontaneous rupture models.

prescribed to vary over the plane of faulting as shown in the figure, with $\Delta\tau$ representing its maximum value. Average dynamic stress-drop in these models turns out to be nearly the same as average static stress-drop, which is an often-quoted seismic source parameter.

Models 1 and 2 represent isolated stress concentrations, while Model 6 represents an assemblage of five discrete stress concentrations. The final fault perimeters for Models 1 and 2 were not prescribed in the calculations; rather, the rupture front decelerated and stopped at the position shown in response to the prescribed stress inhomogeneity. For Model 6, rupture growth was stopped by a prescribed jump in shear strength at the rectangular perimeter shown in the figure.

Rupture velocity turns out to be highly variable for each of the Models 1, 2, and 6, as discussed by Day (1979, 1982b). For example, in each case, the average rupture velocity (final half-length, a , divided by rupture arrival time at the ends of the fault), which is given in the figure, is less than β ; but in each case, local rupture velocity somewhere on the fault exceeds β .

These six earthquake models incorporate a fairly wide range of phenomena: fault length-to-width ratios between 1 and 16/3, uniform versus localized prestress, and constant versus variable rupture velocity. There is considerable observational evidence that variable stress-drop effects are prevalent in shallow earthquakes (for example, Hanks, 1974; Hartzell and Brune, 1979; and Bache, Lambert and Barker, 1980), and the variety of source models used in this study will permit us to make at least qualitative assessments of their importance for seismic discrimination. This is the concern addressed by Blandford (1975), using an ad hoc model for the source spectrum. Our results, based on the above dynamic models, do not agree with his conclusions. In fact, for the models considered here, source complexity tends to reduce the source spectrum near the corner although this reduction may be accompanied by spectral enhancement well above the corner.

Figure 2 shows the far-field P- and S-wave displacement spectra and time histories radiated by these six fault models. For a given fault orientation, the seismic radiation depends on both azimuth and takeoff angle, and the results in Figure 2 are, in each case, for a 45 degree dip-thrust orientation observed at azimuths of ± 90 degrees from the fault strike. Takeoff angles are appropriate to excite teleseismic P-waves at a range of about 35 degrees ($\theta = 27^\circ$ for P-waves, $\theta = 15^\circ$ for S-waves).

Also shown in Figure 2 are the RMS-averaged (over θ and ϕ) spectra for P- and S-waves. The RMS spectra are much simpler than the individual spectra since the focal-sphere averaging has removed spectral holes present for individual rays. They indicate that differences in average spectral shape between P- and S-waves are surprisingly small, particularly for the spontaneous rupture cases. Their smoothness makes the RMS spectra particularly useful for making spectral estimates of body-wave magnitude as is done in a subsequent section. On the other hand, actual body-wave magnitudes are time-domain measurements made from a short segment of the wavetrain, and phase effects may be quite important, particularly for complex waveforms such as those radiated by Model 6. Therefore, we will also use the individual (amplitude and phase) spectra, in combination with synthetic seismogram methods, to make time-domain m_b estimates for the sources.

The spectra and time histories in Figure 2 are shown in non-dimensional form. When we construct spectral and time-domain magnitude estimates, it will be necessary to scale each source function to various values of the fault half-length, a , and maximum stress-drop, $\Delta\tau$. The assumptions implicit in such scaling are described by Day (1982b). In short, we must assume that the following dimensionless quantities are invariant with source size and stress-drop: 1) Poisson's ratio of the source medium, 2) the ratio of fault shear strength to dynamic stress-drop, and 3) the ratio of total fracture energy to total strain energy release. Under these assumptions, the rupture history remains constant as the dimension of the fault is changed.

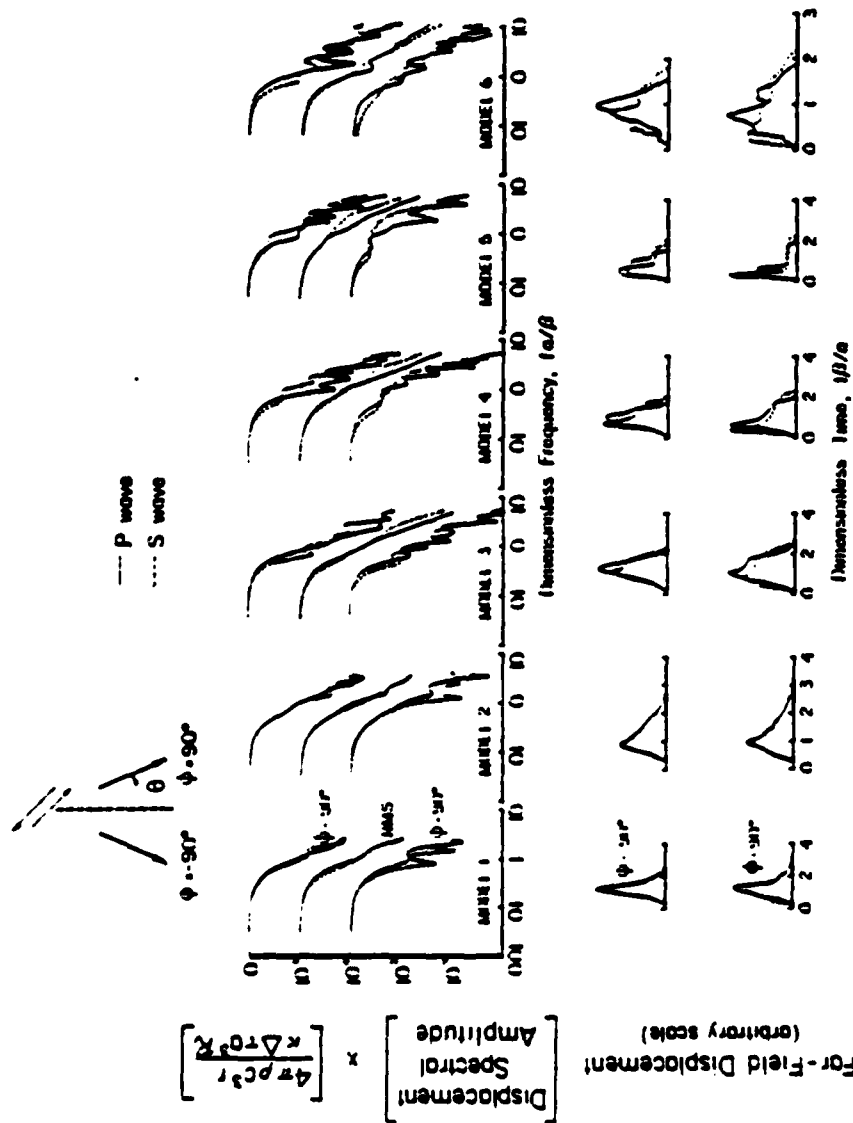


Figure 2. Far-field displacement spectra, and corresponding waveforms at two azimuths for the six theoretical earthquake sources used in the study. Takeoff angles θ are 27° for P-waves 15° for S-waves. Also shown are the RMS averages over takeoff angle θ and azimuth ϕ . The normalization is such that the spectra have unit value at zero frequency. In the normalizing factor, c is the wavespeed α or β , ρ is the density, a the fault half-length, r the hypocentral distance, Δu the maximum dynamic stress-drop, R the double-couple P- or S-wave radiation pattern factor, and κ the dimensionless ratio of seismic moment to $\Delta u a^3$ given in Figure 1 for each source.

As indicated in Figure 2, spectral ordinate varies directly with stress-drop and fault length cubed, and inversely with wavespeed of the source medium cubed, while frequency scales inversely with length and directly with the wavespeed of the source medium. In subsequent analyses, we will set the P- and S-wave speeds of the earthquake source region to 6 km/sec and 3.5 km/sec, and the density to 2.7 gm/cm^3 , values appropriate for granite at mid-crustal depths. Unless otherwise noted, we will set Δ to 100 bars (10 MPa). This value implies average stress drops ranging from 43 bars to 100 bars as shown in Figure 1. With the velocities and stress drop held constant, a simple cube root scaling applies: multiplying the spectral amplitude by a factor A multiplies the corresponding frequency by $A^{-1/3}$.

2.2 EXPLOSION MODELS

We consider two types of explosion source models. The first are one-dimensional (spherically symmetric) finite difference simulations of explosions buried in different geologic materials. The method of computation is described by Cherry, Rimer and Wray (1975). The calculations used here were performed more recently by N. Rimer (unpublished work performed at Systems, Science and Software, 1978-1979) for explosions in dry granite, saturated granite, salt and saturated tuff. The calculation for salt was intended to model the explosion SALMON (yield 5.3 KT). The saturated granite calculation is a model for the explosion PILEDRIVER (yield 60 KT). The tuff model is a typical Nevada Test Site material. The dry granite calculation is a model for French explosions in the Hoggar region of the Sahara. This calculation leads to a very low amplitude reduced velocity potential compared to explosions in the other materials at the same yield.

We use the reduced velocity potential $\dot{\psi}(\omega)$ derived from these calculations to make spectral magnitude estimates and time-domain synthetic seismograms. The reduced velocity potential may be cube root scaled to arbitrary yield: the spectral amplitude scales

directly with yield while the frequency varies as the inverse cube root of the yield. The explosion elastic radius varies directly with the cube root of the yield. Although this scaling may be done for any yield, the numerical calculations were performed for a fixed overburden pressure. In general, larger explosions will be more deeply buried than smaller explosions; so the scaling for $\dot{\psi}$ may not be applicable to explosions at all yields.

For the second explosion source model, we use the empirical source model of Mueller and Murphy (1971). Details of the model are given in Appendix A. This model includes a scaling with depth as well as a scaling with yield (W). The main result of the depth dependence is that the explosion elastic radius varies approximately as $W^{1/5}$ rather than $W^{1/3}$ because of the increasing overburden pressure. We have used Mueller-Murphy reduced velocity potentials for explosions in salt, granite, shale and tuff/rhyolite.

Table 1 gives the material properties of the source media for the eight explosion sources (α = compressional wave velocity, β = shear wave velocity, ρ = density). The long period limit of the reduced velocity potential, ψ_{∞} , and the moment M_0 (defined by $M_0 = 4\pi\rho\alpha^2\psi_{\infty}$) are given for each source scaled to 100 KT. For the Mueller-Murphy sources, depth and overburden pressure are a function of yield; for the finite difference calculations they are fixed.

TABLE 1
PROPERTIES OF EXPLOSIONS SOURCES
(Scaled to 100 KT)

Source	α (km/sec)	β (km/sec)	ρ (kg/m^3)	Depth (m)	Overburden Pressure (bars)	Moment ($\text{NT} \cdot \text{m}$)	V_{∞} (m^3)	Elastic Radius (m)
Numerical Explosions (100 KT):								
Wet Tuff	2400	1300	1915	400	75	6.8×10^{15}	48940	552
Wet Granite	5350	2795	2650	460	120	2.6×10^{16}	26770	705
Dry Granite	5350	2795	2650	460	120	5.8×10^{15}	6100	446
Salt	4550	2540	2200	810	175	3.0×10^{16}	51970	2573
Empirical Explosions (100 KT):								
Tuff/Rhyolite	3500	2021	2000	566	110	1.28×10^{16}	41570	490
Granite	5500	3175	2550	566	140	2.47×10^{16}	25450	780
Salt	4670	2696	2200	566	120	2.71×10^{16}	45000	980
Shale	4320	2495	2350	566	130	1.45×10^{16}	26250	650

III. EFFECT OF SOURCE MECHANISM

As a first step in comparing earthquakes and explosions as generators of body (P) and surface (Rayleigh) waves, we estimate differences in body-wave magnitude (m_b) and surface-wave magnitude (M_s) attributable solely to the difference between double-couple and center-of-dilatation point sources. We neglect, in this comparison, any characteristic differences in source spectrum and source-region material properties.

In a uniform, infinite space, we can write the spectral amplitude of the far-field P-wave radiated by an earthquake, A_b^q , as

$$A_b^q(\omega, \theta, \phi) = \left| \frac{m_q(\omega, \theta, \phi)}{4\pi\rho\alpha^3 r} R_p(\theta, \phi) \right|, \quad (3.1)$$

where $R_p(\theta, \phi)$ is the double-couple radiation pattern factor (with maximum absolute value of 1), $m_q(\omega, \theta, \phi)$ is the earthquake source-spectrum or moment function, ρ is the density, α is the P-wave speed, and r , θ , and ϕ are the spherical coordinates of the receiver relative to the hypocenter. The source-spectrum $m_q(\omega, \theta, \phi)$ contains all the effects of spatial and temporal finiteness of the earthquake (Kostrov, 1968). The long-period limit of the source spectrum, which is independent of θ and ϕ , is the seismic moment of the earthquake, denoted M_0^q .

Similarly, the far-field P-wave spectral amplitude of an underground explosion, A_b^x , is given by (assuming spherical symmetry of the source)

$$A_b^x(\omega) = \left| \frac{m_x(\omega)}{4\pi\rho\alpha^3 r} \right|, \quad (3.2)$$

where $m_x(\omega)$ is the explosion source spectrum. The long-period limit of the source spectrum is the seismic moment of the explosion, M_0^x . The source spectrum $m_x(\omega)$ is proportional to the reduced velocity potential of the explosion, $\dot{\psi}(\omega)$:

$$m_x(\omega) = 4\pi\rho\alpha^2\dot{\psi}(\omega) . \quad (3.3)$$

We now define A_S^q and A_S^x to be the Rayleigh wave spectral amplitudes of the earthquake and explosion, respectively. We define the "relative amplitude factor," X , to be

$$X = \frac{A_S^q/A_S^x}{A_b^q/A_b^x} \quad (3.4)$$

which gives the generation of Rayleigh waves by an earthquake relative to the generation of Rayleigh waves by an explosion of the same body-wave magnitude. Its logarithm, which we call the "relative magnitude factor," is

$$\log_{10} X = (M_S^q - M_S^x) - (m_b^q - m_b^x) , \quad (3.5)$$

which gives the M_S difference ($M_S^q - M_S^x$) for an earthquake and explosion with the same m_b , or the m_b difference ($m_b^x - m_b^q$) for an event pair with the same M_S . In the following analysis, we will be considering distributions of the relative magnitude factor for an ensemble of events. The mean value of $\log_{10} X$, then, will represent the mean distance between the earthquake and explosion populations on the $m_b:M_S$ plane.

We may obtain estimates for the relative amplitude factor using expressions given by Douglas, Hudson and Kambhavi (1971). The earthquake is represented by a point double-couple (dislocation) with fault normal \hat{n} and unit slip vector \hat{s} , located at depth h , and the explosion by a center-of-dilatation located at depth h' . If the earthquake and explosion have the same source spectral shape and the same seismic moment ($m_x(\omega) = m_q(\omega)$), Douglas et al. give the following amplitude ratio for Rayleigh waves:

$$\begin{aligned}
\frac{A_s^q}{A_s^x} &= \frac{\alpha^2}{c_R^2} \exp \left[\frac{\omega_R \eta_\alpha (h' - h)}{c_R} \right] \\
&\times \left| q_0 \left[3 \left(1 - \frac{c_R^2}{2\beta^2} \right) - 3 + \frac{2c_R^2}{\alpha^2} \right] + 2q_1 i \eta_\alpha (1 - E) \right. \\
&\quad \left. + q_2 \left[1 - \left(1 - \frac{c_R^2}{2\beta^2} \right) E \right] \right| \quad (3.6)
\end{aligned}$$

where

ω_R = Rayleigh wave angular frequency

c_R = Rayleigh wave speed

α, β = P and S wave speeds

$\eta_\alpha = (1 - c_R^2/\alpha^2)^{1/2}$

$\eta_\beta = (1 - c_R^2/\beta^2)^{1/2}$

θ = Takeoff angle

ϕ = Azimuth of recording instrument

$q_0 = s_3 n_3$

$q_1 = (s_1 n_3 + s_3 n_1) \cos \phi + (s_2 n_3 + s_3 n_2) \sin \phi$

$q_2 = (s_1 n_1 - s_2 n_2) \cos 2\phi + (s_1 n_2 + s_2 n_1) \sin 2\phi$

$E = \exp \left[\frac{\omega_R h}{c_R} (\eta_\alpha - \eta_\beta) \right]$

For the following analysis, we take $\alpha = \sqrt{3} \beta$, which requires $c_R = .92\beta$.

From equations 3.1 and 3.2, the P-wave amplitude ratio, A_B^q/A_B^x , for events of the same moment and spectral shape, is simply equal to the modulus of the radiation pattern factor, $|R_p|$. This is given by Douglas et al. in the same notation as Equation (3.6):

$$\frac{A_b^q}{A_b^x} = \left| q_0(2 - 3 \sin^2 \theta) + q_1 \sin 2\theta + q_2 \sin^2 \theta \right|. \quad (3.7)$$

These expressions apply to a uniform half-space, and will be the basis for the analysis which follows in this section. Equation 3.7 neglects effects of surface-reflected waves. Modifications introduced by reflected phases and near-source material properties will be reviewed in later sections.

Douglas et al. used Equations 3.6 and 3.7 to estimate the effects of the source mechanism on the relative magnitude factor. Some of the conclusions of the Douglas et al. paper, however, depend rather strongly on the choice of a very small takeoff angle of 10 degrees and on the limited number of source orientations considered. This takeoff angle is appropriate for a source-layer P-velocity of 3 km/second for an observation point located 65 degrees away. This assumption led to the conclusion that a shallow, vertical dip-slip fault is a more efficient generator of surface waves compared to body waves than a 45 degree dip-slip fault. This result arises because the assumed takeoff angle is close to $\theta = 0$, which is a P-wave node for the vertical dip-slip fault and an antinode for the 45 degree dip-slip. A more appropriate crustal compressional velocity for all but the shallowest of earthquakes is about 6 km/second. This requires takeoff angles of between 29 degrees and 17 degrees for an observation distance range of 30 degrees to 80 degrees (Richter, 1958).

In Table 2, we have listed the relative amplitude factors for vertical dip-slip, 45 degree dip-slip, and strike-slip double-couples using an explosion depth of one kilometer. We have used $\alpha = 6$ km/sec, a period of 20 seconds, and azimuths of 90 degrees for the dip-slip events and 45 degrees for the strike-slip events (all maxima of the Rayleigh wave radiation pattern). The numbers on the table must be divided by $\sin 2\theta$, $\cos 2\theta$, and $\sin^2 \theta$ respectively to include the effect of the body wave radiation

TABLE 2

RELATIVE AMPLITUDE FACTORS FOR POINT DISLOCATIONS

<u>Earthquake Depth (km)</u>	<u>Vertical Dip Slip</u>	<u>45° Dip Slip</u>	<u>Strike Slip</u>
1	.27	1.80	1.40
5	.79	.70	.70
10	1.60	.15	.16
15	1.80	.60	.14
20	1.80	.80	.30
25	1.70	.88	.37
30	1.50	.86	.38

pattern. The three sources behave very differently with changes in depth. For very shallow (< 5 km) sources, the 45 degree dip-slip and strike-slip events are much more efficient generators of surface waves than the vertical dip-slip events. On the other hand, for depths greater than 5 km, the vertical dip-slip becomes a more efficient generator of surface waves. The 45 degree dip-slip and strike-slip pass through a node and are very inefficient surface wave generators at about 10 km depth.

In order to avoid biases associated with specific source orientations, we examine the frequency distribution of the relative amplitude factor for each of several ensembles of earthquakes. In each ensemble, it is assumed that the distribution of fault orientations is uniform in the sense that observations at a given takeoff angle and azimuth sample the focal sphere uniformly. Figure 3 shows the resulting distribution functions of the relative magnitude factor, calculated from Equations 3.6 and 3.7, for each of several earthquake source depths and takeoff angles. The explosion source depth is 1 km in each case. Recall that the horizontal axis represents the estimated separation in the $m_b:M_s$ plane between an explosion and an earthquake of the same m_b (or the same M_s). The vertical axis can be thought of as the relative number of observations of event pairs with a given separation when effects of source spectrum, source region material properties, and reflected phases are neglected.

The distributions in Figure 3 are surprisingly smooth. Although the excitation of Rayleigh waves relative to P-waves for a particular fault orientation is quite sensitive to source depth and takeoff angle, the distribution of the relative excitation over a range of fault orientations is not very sensitive to source depth or takeoff angle. The average separation of the populations due to source mechanism is only about one third of a magnitude, and about one third of the observations have a relative magnitude factor less than zero.

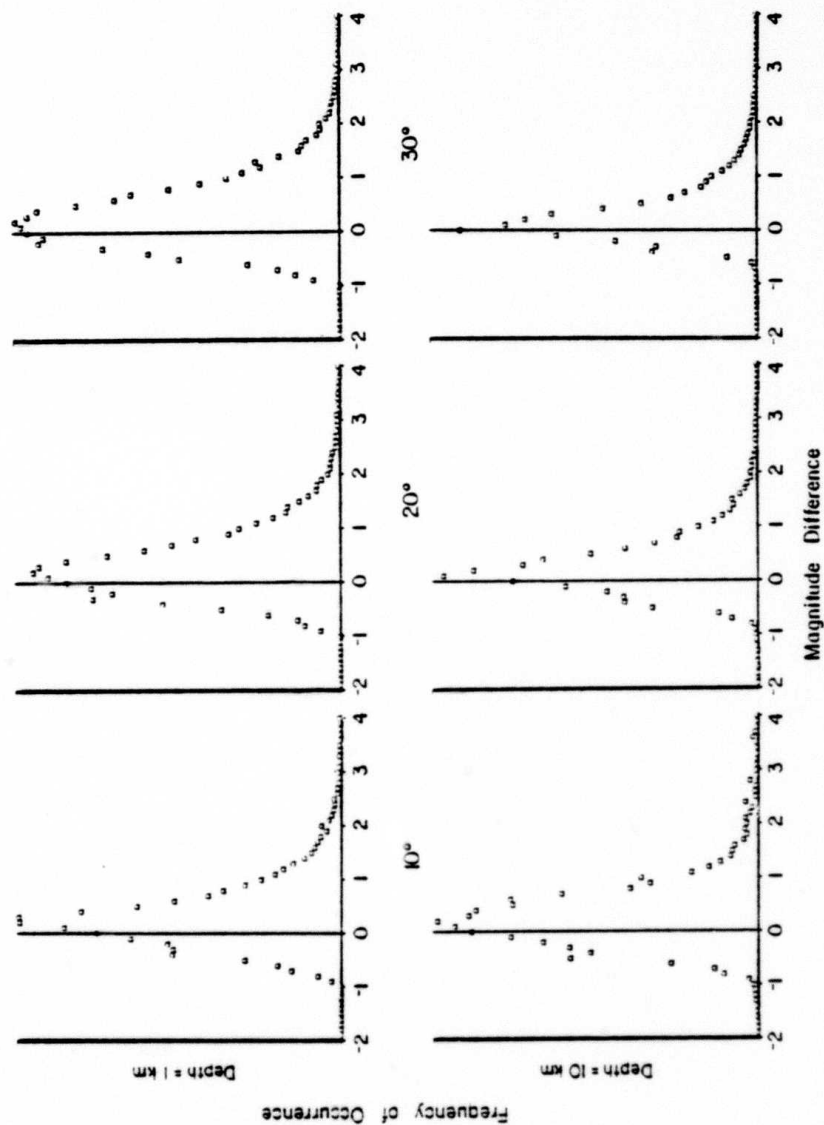


Figure 3. Distribution of magnitude differences for several depths and takeoff angles. Horizontal axis is $M_S(\text{earthquake}) - M_S(\text{explosion}) - m_B(\text{explosion})$ (single station measurements). Vertical axis is the number of pairs of events with this magnitude difference. A uniform distribution of dip and rake angles and observation azimuths were used for each figure. Top row is for both earthquake and explosion at a 1 km depth. Bottom row is for an earthquake at 10 km and an explosion at 1 km. The three figures on each row are for takeoff angles of 10°, 20° and 30° respectively.

The values of m_b and M_s used in discrimination studies are usually averages of m_b and M_s over a range of observation azimuths. If we adopt this approach, and average the theoretical Rayleigh wave and body wave magnitudes separately instead of looking at individual stations, then we get a more realistic estimate for m_b and M_s . We can also consider a range of depths and takeoff angles. Figure 4 shows the distribution function for event pairs with M_s and m_b averaged over azimuth for earthquakes uniformly distributed in source depth (1 to 25 km) and takeoff angle (10 to 30 degrees) as well as in source orientation. Points very close to nodes (less than 5 percent of the maximum amplitude) were not used in the average of magnitudes over azimuth. The result is a narrower distribution function sharply peaked at about .3 - .4 magnitude. The average over azimuth removes the extremes which may be seen in individual observations resulting from observation points close to nodes in the body or surface wave radiation patterns.

We can see the individual contributions of M_s differences and m_b differences by computing M_s and m_b separately using Equations 3.6 and 3.7 and plotting a two-dimensional distribution. The contour plot in Figure 5 shows the frequency of events as a function of M_s difference and m_b difference for earthquakes and explosions with the same moment. Again, these distributions are for a range of depths and takeoff angles and are averaged over azimuth. For all event pairs, m_b of the explosion exceeds m_b of the earthquake. This is simply a result of the radiation pattern difference mentioned before. A more surprising result is that earthquakes have slightly smaller M_s values than explosions with the same moment. The distributions are strongly concentrated about the point $M_s^q - M_s^x = -.1$, $m_b^q - m_b^x = -.45$. Fifty percent of the event pairs are located in the interval $-.3 \leq M_s^q - M_s^x \leq 0.$, $-.6 < m_b^q - m_b^x < -.3$. About 20 percent of event pairs have $M_s^q - M_s^x - (m_b^q - m_b^x) \leq 0$, and cannot be discriminated by source mechanism alone.

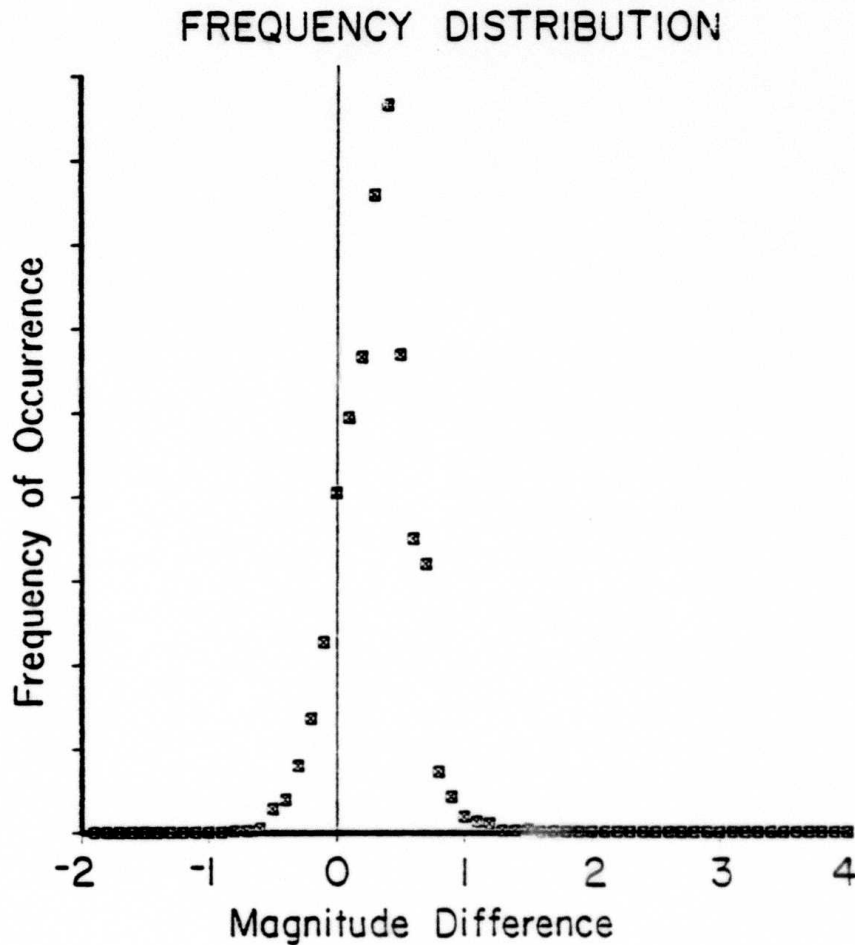


Figure 4. Frequency distribution of the difference between earthquake and explosion magnitudes due to source mechanism (double-couple versus dilatation) alone. The horizontal axis is the function $M_s(\text{earthquake}) - M_s(\text{explosion}) - (m_b(\text{earthquakes}) - m_b(\text{explosion}))$. For two earthquakes with the same M_s , it represents the amount by which $m_b(\text{explosion})$ exceeds $m_b(\text{earthquake})$. The vertical axis is the number of earthquakes/explosions which fall into a given magnitude difference using a range of depths (1-25 km), source orientations (all), and takeoff angles (10°-30°). Surface and body wave magnitudes were averaged over azimuth.

We find the following relations for the average event pair with the same moment:

$$\overline{(M_S^Q - M_S^X)} \approx -.1$$

$$\overline{(m_B^X - m_B^Q)} \approx .45$$

and in general:

$$\log_{10} X = \overline{(M_S^Q - M_S^X)} - \overline{(m_B^Q - m_B^X)} \approx .35 \quad (3.8)$$

This result is surprisingly stable. We have performed this calculation for several other depth ranges (5-10 km, 15-20 km, and 25-50 km) and find that although the shape of the distribution (Figure 5) varies somewhat, the peak of distribution always occurs in a narrow range with $\log_{10} X \approx .35$.

For small events, there will be an observational bias in favor of larger amplitude arrivals. Small amplitude body and surface wave arrivals may not be reported. Both body and surface wave magnitudes are likely to be overestimated. If body and surface waves are observed only near their radiation pattern maxima, then the source mechanism effect is reduced to $\log_{10} X \approx .2$.

Our final result of .35 for the magnitude difference is similar to Gilbert's (1973) estimate of .52, but the interpretation is quite different. He suggested that for a given moment, body wave magnitudes should be almost equal while surface wave magnitudes should be greater for earthquakes. Gilbert's analysis depends on approximating the double dot product of two tensors by the product of their Euclidian norms. Apparently, this procedure does not yield good separate estimates of Rayleigh and P-wave excitation by earthquakes relative to explosions (i.e., A_S^Q/A_S^X and A_B^Q/A_B^X), though it does give a reasonable estimate of the relative amplitude factor X .

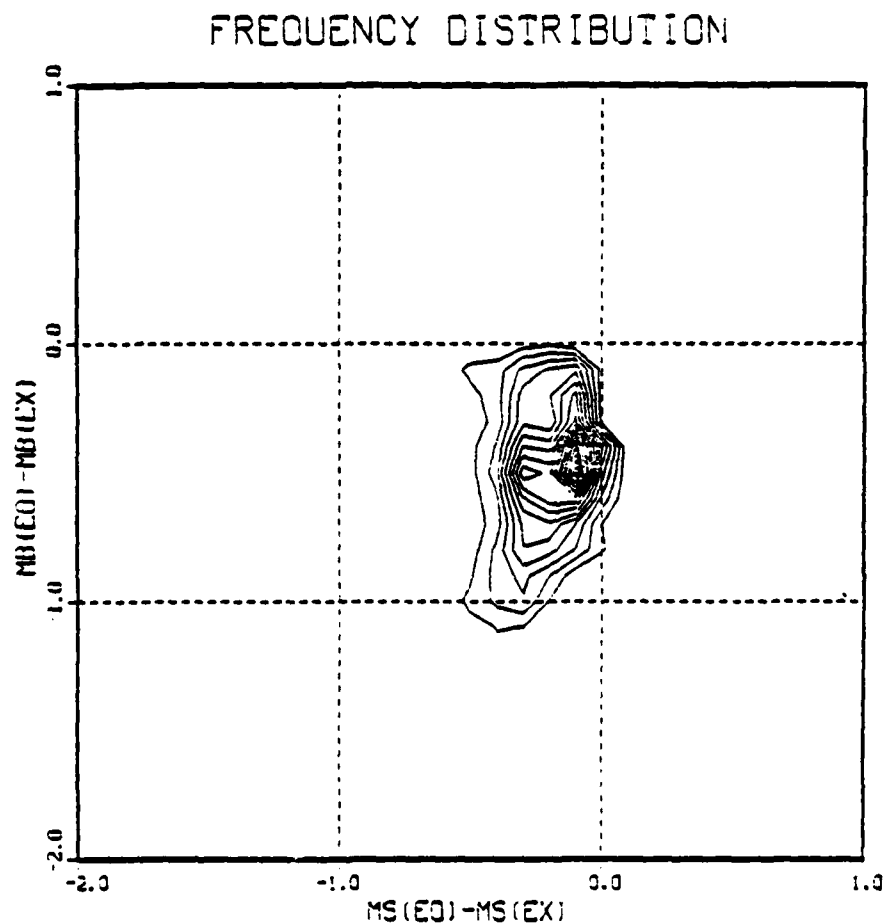


Figure 5. Contour plot of frequency distribution in m_b/M_s plane. Vertical axis is the difference between m_b of earthquakes and m_b of explosions. Horizontal axis is difference between M_s of earthquakes and M_s of explosions. In general, explosions have slightly higher M_s and substantially higher m_b than earthquakes with the same moment. The frequency of occurrence of event pairs on the outermost contour is 5 percent of the maximum. Inner contours are multiples of 5 percent.

Figures 4 and 5 represent our best estimate of the difference between, and dispersion of, the earthquake and explosion populations based on source mechanism alone. Clearly, source mechanism makes a significant contribution, but is not sufficient to explain observed differences between m_b and M_s of earthquakes and explosions. The width of the distribution function does explain why there should be more scatter in the earthquake population and why earthquakes may occasionally look like explosions.

IV. EFFECT OF DEPTH

The depth of the source can affect both body and surface wave generation. The most important effect of depth is interference caused by reflected phases. The pP phase from an explosion is almost identical to direct P but opposite in sign and delayed in time. The spectral amplitude is changed by a factor of:

$$\left| 1 + A_1 \exp(- (2i \omega_p h'/\alpha) \cos\theta) \right| \quad (4.1)$$

where A_1 is the reflection coefficient of the free surface and ω_p is the angular frequency of the P-wave. For steeply descending rays in an elastic half-space $A_1 \approx -1$. If the spectrum of the direct P-wave is $g(\omega)$, the spectral amplitude of P + pP is given approximately by:

$$\left| g_t(\omega) \right| \approx 2 \left| g(\omega) \right| \left| \sin \frac{\omega \tau}{2} \right| \quad (4.2)$$

where τ is the delay time $\tau \approx 2h'/\alpha$. At low frequencies there is complete cancellation while at frequencies of $f = \omega/2\pi = (2n + 1)/2\tau$ where n is an integer, the amplitude is doubled (Figure 6). There will be cancellation again at $f = n/\tau$. Bache, Day and Savino (1979) found time delays for a series of NTS explosions, with m_b ranging from 5.5 to 6.5, to range from 0.6 seconds to 1.0 seconds. A shallow explosion in a high velocity material such as PILEDRIVER could have a time delay as short as 0.2 seconds. A deep explosion in a low velocity material could have a time delay as long as 2 seconds. Obviously this can be very important to m_b measurements and to VFM discrimination. In practice, for moderate sized explosions, interference of pP is more likely to increase m_b than to decrease it. The reason is that the amplitude will be measured directly from the seismogram and then divided by the instrument response corresponding to the measured frequency. This frequency will move away from a minimum and toward a local maximum.

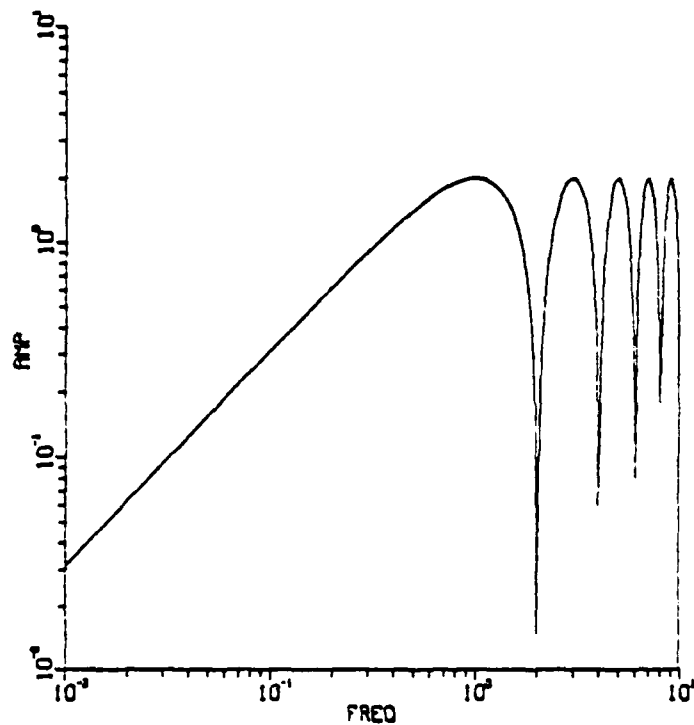


Figure 6. Spectral amplitude of direct P plus elastic pP with a time delay of 0.5 seconds. The two waves interfere destructively at low frequencies and alternately interfere constructively and destructively at high frequencies. The spectrum of the far field P-wave is the spectrum of the direct P-wave multiplied by this function.

The effect of reflected phases on earthquake P-waves is more complex, but in most cases less important. If the earthquake is more than a few kilometers deep, the reflected phases will be separated in time from the direct P-wave. Because of the radiation pattern difference, P and pP will usually not have the same amplitude. Only for a few preferred fault orientations will there be strong destructive or constructive interference.

In this analysis and subsequent examples, we use a linear, elastic reflection coefficient to determine pP. In fact, the upgoing and reflected P-waves from underground explosions travel through a highly cracked region and, in most cases, cause spallation of the upper layers. The resulting effect on far field body waves is not well-determined at present. Bache, Day, and Savino (1979) in a study of NTS explosions estimated that nonlinear effects reduce pP by a factor of 0.5 - 0.75. On the other hand, Burdick and Helmberger (1979), using Russian explosions, found that the body waves could be modeled using a linear pP. Day, Rimer, and Cherry (1982) show that conservation of momentum requires that nonlinear effects leave pP unchanged at long periods. The most likely effect of nonlinearities is attenuation of pP at high frequencies. This may reduce the amount of interference with direct P.

For small explosions, interference of pP is likely to reduce m_b . Using the Mueller-Murphy empirical relation for depth $h = .122W^{1/3}$ km, the travel time delay is

$$\tau = \frac{.244W^{1/3}}{\alpha} \quad \text{seconds.}$$

This will cause destructive interference at 1 Hz for yields of 50 KT or less in granite and for 5 KT or less in tuff.

The effect of pP interference is to increase the separation of the earthquake and explosion populations on the $m_b:M_s$ plane for moderate and high yields by as much as .3, and to reduce the

separation at low yields. This causes an apparent convergence of the populations at small magnitudes which will be evident in the synthetic seismogram results presented in a later section.

The effect of reflected phases on the variable frequency magnitude discriminant is the opposite of the effect on the $m_b:M_s$ discriminant. A summary of the VFM method is given by Bache, Day and Savino (1979). The method consists of applying a "comb" of narrow band filters over a range of frequencies from 0.4 Hz to 4.0 Hz to a short-period seismogram. Magnitude measurements are then made at two frequencies as far apart as noise will permit -- usually about 0.5 Hz and 3.0 Hz. In practice, the spectra are smoothed to remove some of the dips in the spectra. This has the result that interference of pP tends to amplify the spectra, especially at higher frequencies. If the first interference peak occurs at 0.5 Hz or less, the effects should average out and cause no apparent amplification. On the other hand, for small events, destructive interference at 0.5 Hz will reduce the low frequency amplitude for shallow explosions with pP - P time delays less than about 0.3 seconds, increasing the separation by as much as 0.5. Thus, the interference of pP will aid in the explosion identification using the VFM discriminant, and hinder the identification using $m_b:M_s$. For deeper events, however, interference of pP will help in the identification of explosions by $m_b:M_s$ and complicate the identification (by adding spectral dips and peaks) using the VFM discriminant.

Surface wave generation is also affected by source depth. A vertical dip-slip earthquake at the surface causes no surface wave generation. A strike slip or 45 degree thrust earthquake at a critical depth, or observed at a critical frequency given approximately by $\omega h \approx c_R$, also causes no surface wave generation (This is true for a layered half-space as well as for a uniform half-space although the critical depths will be different. See Table 2). In Figure 7 we have plotted the relative magnitude factor (from Equation 3.5) as a function of frequency for strike slip and

FREQUENCY DEPENDENCE OF RAYLEIGH GENERATION

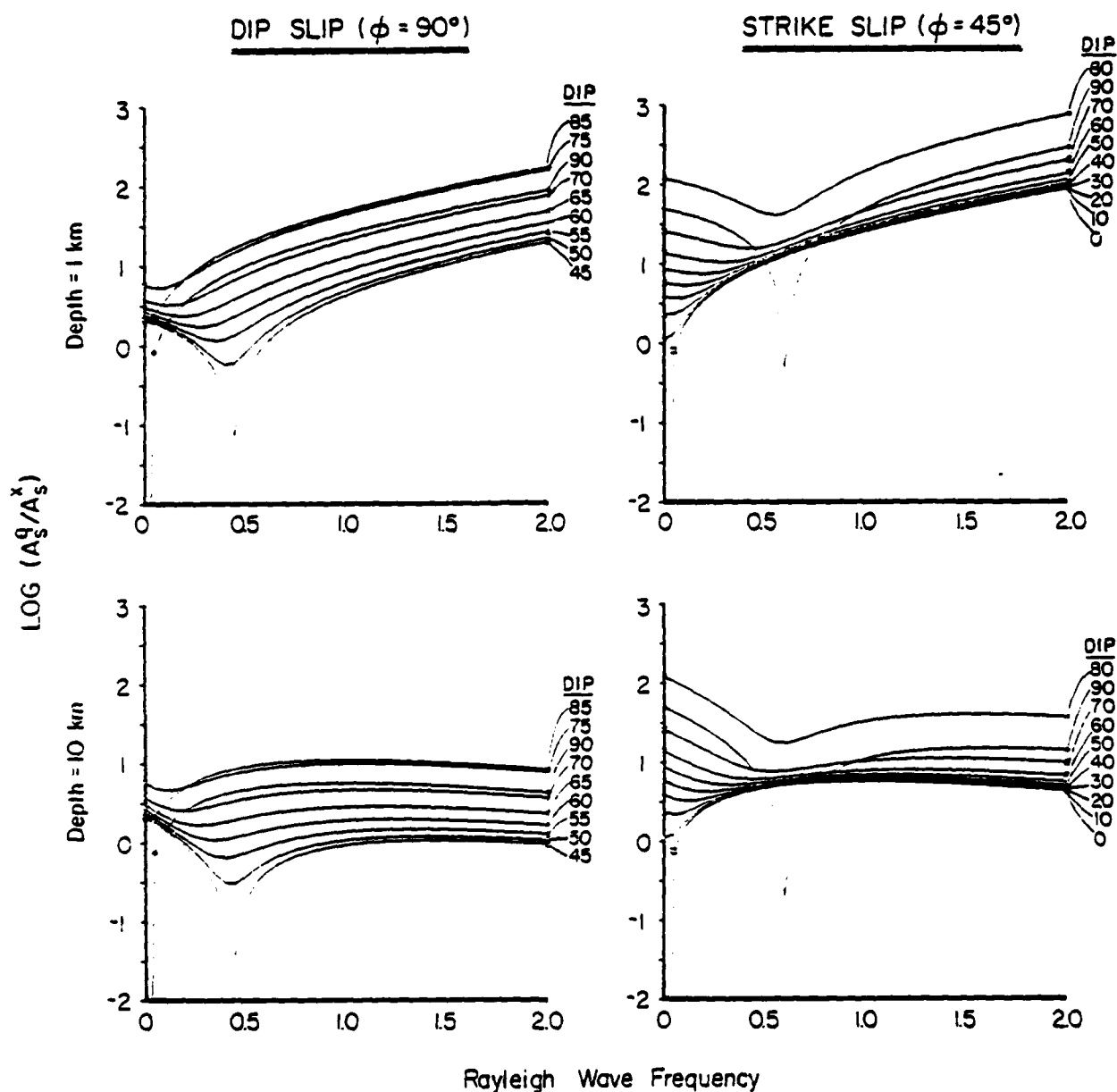


Figure 7. Relative Rayleigh wave amplitudes as a function of frequency, depth and dip angle. Observation point for dip-slip is 90° , for strike-slip 45° close to maxima in the radiation pattern. Takeoff angle for body waves is 10° (body waves are not frequency dependent). The Rayleigh wave velocity is 3.185 km/sec. Vertical axis is $\log(A_S^q/A_S^x)$ for same body wave amplitude.

dip-slip earthquakes at two depths, for a number of dip angles. There is a clear frequency and depth dependence to the Rayleigh wave amplitude. Tsai and Aki (1971) suggested that this depth/frequency dependence could be used to discriminate earthquakes from explosions. Unfortunately, as Figure 7 shows, the frequency dependence is different for different depths and different double-couple orientations. In particular, the dips in the spectrum are only obvious for source orientations close to vertical strike slip, vertical dip-slip, or 45 degree dip-slip. The spectrum is relatively smooth and homogeneous at intermediate orientations.

It is customary in source studies to consider these three source orientations individually and then to make conclusions based on the results using the fact that all double-couple sources are linear combinations of these. As we have seen, however, these particular source orientations have some anomalous features which, in general, do not occur for linear combinations of the sources; so care is needed in making general conclusions from properties of these sources alone.

V. EFFECT OF SOURCE REGION ELASTIC PROPERTIES

We have shown that source mechanism and source depth can explain part, but not all, of the observed $m_b - M_s$ difference between earthquakes and explosions. Source depth can also explain part of the difference found using the VFM discriminant. The remaining differences may be explained by differences in the source spectra and the material properties of the source region. In this section we consider the effects of the latter.

Actually the near-surface geologic structure has two very different influences on the explosion signal which we must distinguish. First, the nonlinear rheology of the medium affects the explosion source spectrum. This effect is considered in the next section. In this section, we are concerned with the manner in which near-source elastic properties modify transmission of the explosion signal. Here, we take a simplified view of the wave propagation in order to estimate this transmission effect alone. In a later section, we compute synthetic seismograms which incorporate the effect of crustal geology rigorously.

We model the source region as a layer of lower velocity material over a half-space. We restrict attention to explosions and earthquakes occurring in the same general area; so we will not concern ourselves with the travel path outside of the source region. Since earthquakes are, in general, deeper than explosions, we will consider the earthquakes to be located in the half-space while explosions will be located in the overlying layer.

We need to estimate the body wave and surface wave amplitudes for an explosion or earthquake in this two layered structure. We will consider only the direct (far-field) P-wave since reflected phases have been considered separately. For the earthquake, the body wave will be equal to the free space body wave for which the spectral amplitude A_b^q is given by Equation 3.1. For the explosion, however, the free-field body wave, Equation 3.2, is

modified by the transmission coefficient from the upper to the lower layer. For steeply descending rays, the transmission coefficient (T_{xq}) is approximately

$$T_{xq} = \frac{2\alpha_x^2 \rho_x}{\alpha_q (\rho_x \alpha_x + \rho_q \alpha_q)}$$

where ρ_q and α_q are the density and P-wave velocity of the half-space and ρ_x and α_x are the density and P-wave velocity of the layer (Cerveny and Ravindra, 1971). The continuous limit (gradual transition between materials) may also be found using WKBJ theory (Aki and Richards, Chapter 9, page 424). The body wave spectrum from a source with spectrum $m_x(\omega)$ is given for a steeply descending ray by

$$u(\omega) = \frac{m_x(\omega)}{4\pi [\rho_q \alpha_q \rho_x \alpha_x^5]^{1/2} R} \quad (5.1)$$

where R is a geometrical spreading factor. In our case,

$$R = \frac{\alpha_q}{\alpha_x} r$$

The amplitude $|u(\omega)|$ is the explosion body wave amplitude A_b^x . Comparing with Equation 3.2, we find that the transmission coefficient is

$$T_{xq} = \sqrt{\frac{\rho_x \alpha_x^3}{\rho_q \alpha_q}} \quad (5.2)$$

These two transmission coefficients are similar in amplitude, especially for velocity differences of less than a factor of two. We will use the continuous coefficient because of its simpler form.

Aki and Richards (1980, Chapter 7) give a general expression for the excitation of surface waves by a source with a given seismic moment tensor in terms of the free eigenfunctions of a layered medium. For the case of an explosion, the Rayleigh wave amplitude is given by

$$u_x = F(r) \left[Kr_1(h) \frac{2\beta^2}{\alpha^2} + \frac{r_4(h)}{\rho\alpha^2} \right] m_x(\omega) \quad (5.3)$$

where $F(r)$ is a propagation function, K is the Rayleigh wave number, α , β , and ρ are the P-wave and S-wave velocities and density of the source material, h is the source depth and r_1 and r_4 are, respectively, horizontal displacement and normal stress eigenfunctions of the layered space. The stress eigenfunction r_4 vanishes at the free surface. For periods at which M_s is measured (about 20 seconds), r_4 is small for all normal explosion depths. Furthermore, at such periods, r_1 is nearly equal to the half-space eigenfunction. Also, we can neglect the effect of source material on explosion source spectral shape at these long periods. The amplitude of surface waves generated by explosions in different materials will therefore be proportional to $M_0^x \beta^2 / \alpha^2$. For different media with similar Poisson's ratios, the amplitude of surface waves generated by explosions will be proportional to the explosion moment M_0^x .

Combining the results for body and surface waves, we find that the contribution of source-region material properties alone to the relative amplitude factor is given by

$$\frac{A_s^q / A_s^x}{A_b^q / A_b^x} = \left(\frac{\rho_q \alpha_q^3}{\rho_x \alpha_x^3} \right)^{1/2} \quad (5.4)$$

The logarithm of this number is the contribution of source-region elastic properties alone to the distance between the earthquake and explosion populations on an $m_b:M_s$ diagram. It is added to the separation found before due to radiation pattern which was estimated

earlier. This contribution can be very significant. For explosions in low velocity materials such as tuff, it can increase the magnitude difference by about .6, assuming that earthquakes generally occur in the crystalline basement.

VI. SPECTRAL COMPARISON OF SOURCES

In this section we will make synthetic $m_b:M_s$ curves and synthetic VFM curves by combining the contributions analyzed in the previous sections. That analysis is sufficient to give estimates of relative spectral amplitude. The first step in the synthesis is to turn these relative spectral amplitudes into estimates of body and surface wave magnitudes. To do this we need at least one reference point. We use the result of Murphy (1977), based on NTS data, that a 100 KT explosion in a tuff/rhyolite medium has an m_b of 5.5 and an M_s of 4.0. Using these values and the spectrum for the Mueller-Murphy Tuff/Rhyolite explosion source, we can scale all of the explosions:

$$m_b^q = \log_{10} (A_b^x) + C_b^x \quad (a)$$

(6.1)

$$M_s^x = \log_{10} (A_s^x) + C_s^x \quad (b)$$

where the constants C_b^x and C_s^x are chosen to give agreement with Murphy's result for 100 KT. In this section, we will approximate A_b^x using Equation 5.1 so that both the source spectrum and the source region transmission properties are accounted for. As discussed in the last section, we can simply take A_s^x proportional to the source spectrum m_x .

For earthquakes, we use expressions analogous to Equation 6.1, but modify the constants to include the effects of source mechanism and radiation pattern. For m_b^q and M_s^q , we write

$$m_b^q = \log_{10} A_b^q + C_b^q \quad (a)$$

(6.2)

$$M_s^q = \log_{10} A_s^q + C_s^q \quad (b)$$

and from our earlier analysis we know that $C_b^x \approx C_b^q + .45$ and $C_s^x \approx C_s^q + .1$. We will evaluate A_b^q and A_s^q from the theoretical RMS earthquake spectra.

The functions A_b are evaluated at a period of one second while A_s are evaluated at 20 seconds. These amplitudes will, of course, vary from the measured time-domain amplitude because of the finite spectral width of the seismometer response, but we will assume for now that this is an adequate approximation. In the next section we will use synthetic seismograms to test this approximation.

Using MKS units for all quantities and using unit distance for the body waves, we find the constants in Equations 6.1 and 6.2 to be

$$C_b^x \approx 4.75$$

$$C_b^q \approx 4.3$$

$$C_s^x \approx -12.1$$

$$C_s^q \approx -12.2 \quad ;$$

since, in the long period limit, the surface wave amplitudes are proportional to the seismic moment, this also gives a moment/magnitude relation. For small explosions

$$M_s^x \approx \log_{10} M_0^x - 12.1 \quad (6.3)$$

and for small earthquakes:

$$M_s^q \approx \log_{10} M_0^q - 12.2 \quad . \quad (6.4)$$

We can compare $M_s:M_0$ relations obtained from Equations 6.1 and 6.2 with empirical observations of M_s and moment. Figure 8 shows measurements for a large number of earthquakes using data from Kanamori and Anderson (1975) and Hanks and Kanamori (1979). The solid curves on the figures are the theoretical values of M_s computed from Equation 6.2 using the 6 finite difference earthquake calculations. In general, agreement with the earthquake observations is quite good in spite of the fact that we normalized

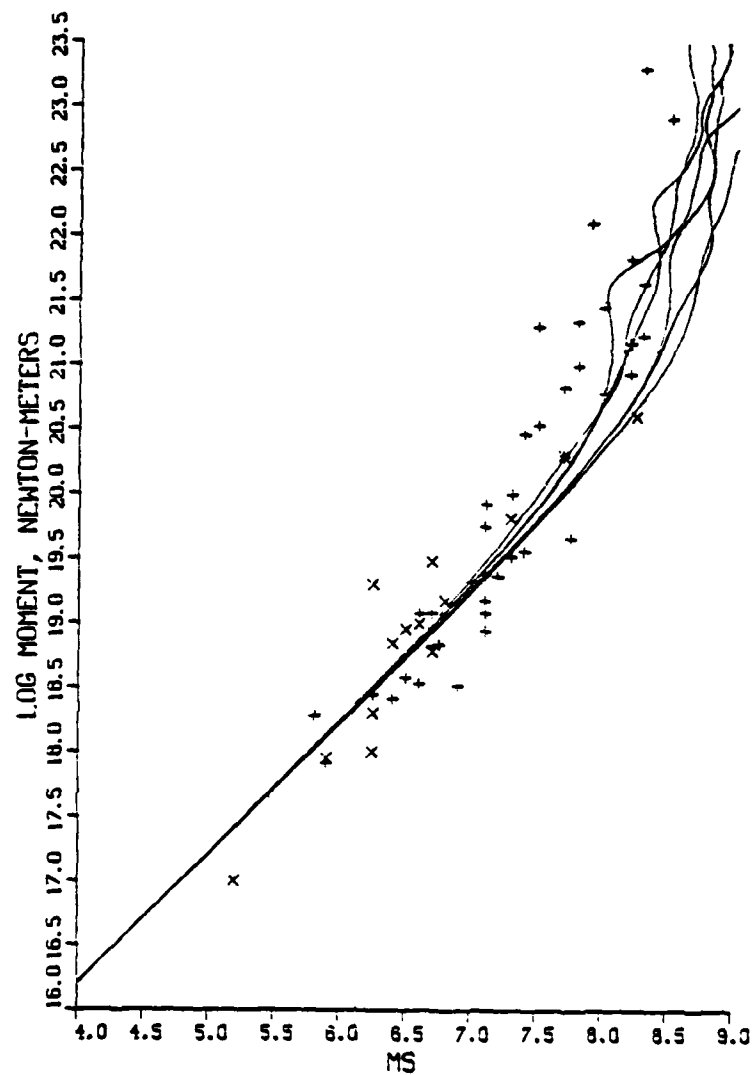


Figure 8. Moment versus surface wave magnitude. M_s is computed from the scaled 20 second amplitude for the six earthquake spectra. Data points are from Kanamori and Anderson, 1975 (+) and Hanks and Kanamori, 1979 (x).

our magnitudes to an explosion model. Geller (1976), using a Haskell dislocation model and the same data set, estimated $C_S^Q \approx -11.9$.

A simple Haskell dislocation model predicts a slope of one at small magnitudes followed by a slope of $3/2$ at intermediate magnitudes, and, eventually, an infinite slope on the moment/magnitude plot. Kanamori and Anderson (1975) determined that the slope should be $3/2$ for most events with M_S between 6 and 8, and used this relation to estimate stress drops. Our results do not show a clear slope of $3/2$ at any point. In fact, the slopes are nearly one for $M_S \leq 7$ for all theoretical curves and become very steep in an irregular manner for larger earthquakes. For $M_S < 7$, therefore, the curves are very insensitive to changes in stress drop.

We can now compute synthetic $m_b:M_S$ curves using Equations 6.1 and 6.2 for all of the explosion and earthquake models. The result is shown in Figure 9. These synthetic curves include effects of source spectrum, source region transmission properties, and average source mechanism, but include no correction for interference by surface-reflected phases. The solid lines on the figure are the earthquake models; the dashed lines are the finite difference explosion models; and the dotted lines are Mueller-Murphy explosion models. The explosion population is very well separated from the earthquake population even at small magnitudes. There is, of course, much more scatter in the earthquake population than is shown since we have used only the peak of the source mechanism frequency distribution (Figure 4). An interesting observation is that for most sources, spectral differences are of secondary importance for events with $M_S < 4$.

As mentioned earlier, fault mechanism is responsible for an average difference of about .35 between the populations. At small magnitudes, most of the remaining difference is due to variations in source material properties as discussed earlier. The surface to body wave amplitude ratio A_S/A_B is proportional to $\sqrt{\rho a^3}$; so an explosion in a lower velocity material has M_S decreased

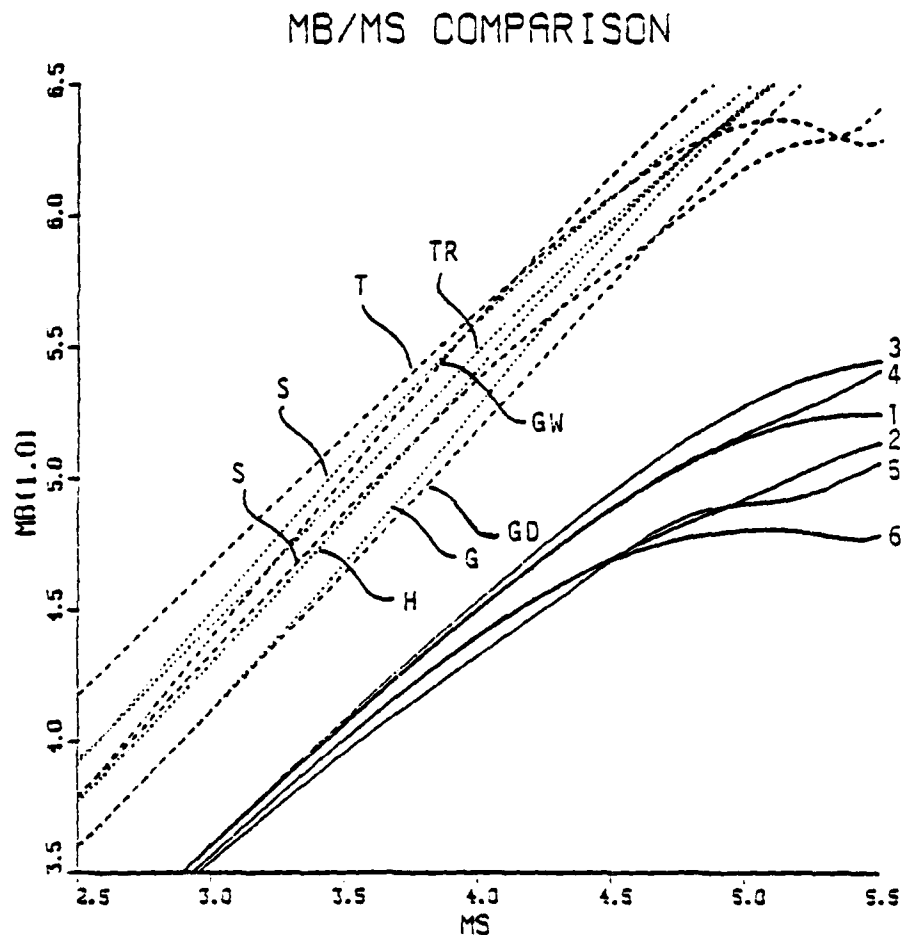


Figure 9. $m_b:M_s$ comparison using source spectra at one and twenty seconds. Earthquakes (solid lines) are identified by number as in Figure 1. Mueller-Murphy explosion sources (dotted lines) are for Salt (S), Granite (G), Tuff-Rhyolite (TR) and Shale (H). Numerical explosion sources (dashed lines) are for Salt (S), Dry Granite (GD), Wet Granite (GW) and Tuff (T). The theoretical curves compare well with the data of Marshall and Basham (1972). Separation between the populations at low magnitude is due primarily to source mechanism and source region elastic properties. This figure does not include interference of pP and uses only the peak source mechanism effect. The distribution in Figure 4 must be superimposed on the earthquake curves.

relative to m_b . This accounts for an average magnitude difference of 0.4 - 1.0 even in the absence of spectral differences. Figure 8 is in very good agreement with the empirical data of Marshall and Basham (1972, Figures 6 and 8).

Although source spectral differences may be of secondary importance to $m_b:M_s$ discrimination, they are of primary importance to VFM discrimination. Figures 10 to 12 are comparisons of spectra of individual earthquake models and explosion models. The explosion models were all evaluated at 100 KT, and earthquake models were scaled to have the same P-wave spectral amplitude, in the long period limit, as the 100 KT explosion. For the purpose of these comparisons, radiation pattern effects were neglected ($c_b^q = c_b^x$), and the maximum earthquake P-wave amplitude is used. The earthquake spectral amplitudes are root mean square spectral amplitudes normalized to the maximum of the radiation pattern. The solid line on each figure is the logarithm of the P-wave spectral ratio (explosion to earthquake). The normalization requires that this ratio equal one in the long period limit. Also shown on the figures are the individual explosion (dashed) and earthquake (dotted) spectra normalized to one at long period.

These figures show clearly why VFM works as a discriminant. In all cases the explosions have significantly more high frequency energy than the earthquakes. In the first set of figures, Figure 10 shows the Mueller-Murphy tuff/rhyolite explosion spectrum (at 100 KT) compared to each of the earthquake sources while Figure 11 shows earthquake source number 1, the spontaneous rupture with a 100 bar stress-drop in a circular region surrounded by a zero stress-drop region, compared with the four numerical explosion sources. Figure 12 shows earthquake number 1 compared with the four empirical (Mueller-Murphy) explosion sources.

The earthquake and numerical explosion sources may be scaled directly to other yields by simply translating the axis by $1/3 \log_{10}(W/100)$. Scaling for the Mueller-Murphy sources is more complicated (see Appendix A), and these sources become more

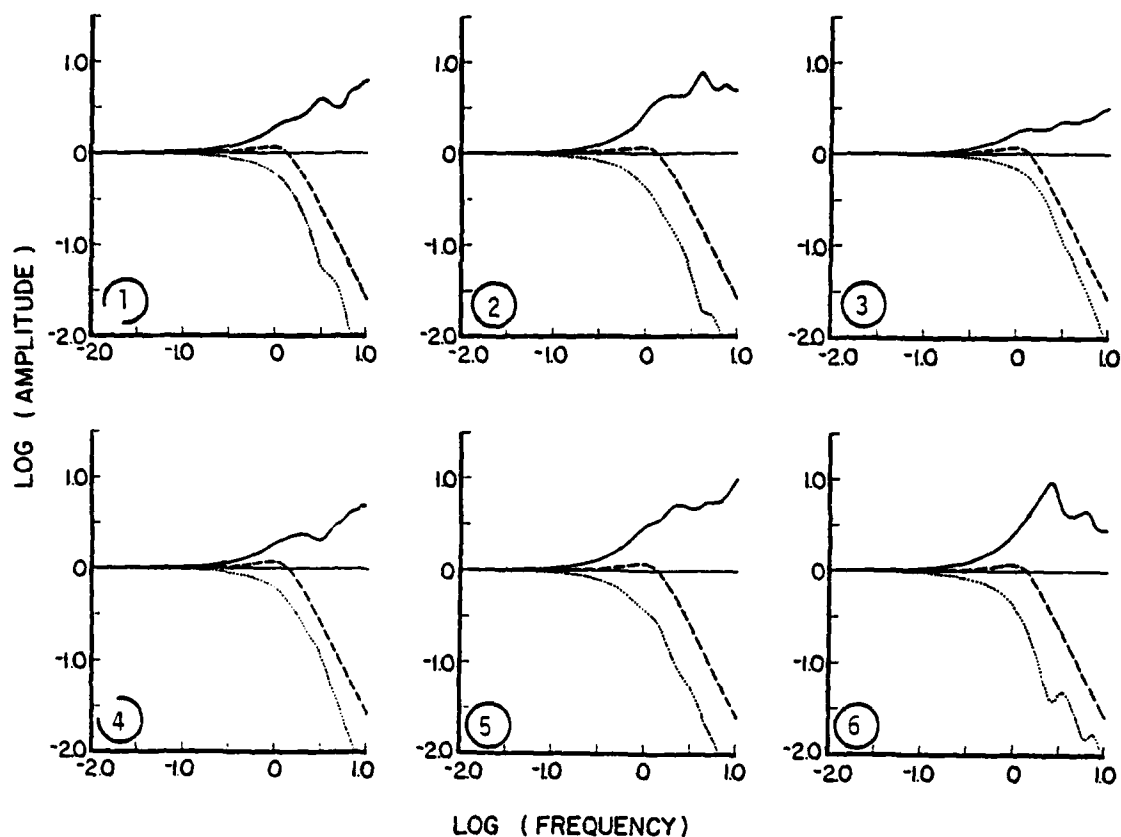


Figure 10. Spectral comparison of earthquake sources with a 100 KT explosion in Tuff (Mueller-Murphy). Dotted line is earthquake RMS spectrum observed at a radiation pattern maximum and normalized to same long period body wave limit as the explosion body wave. Dashed line is the explosion P-wave spectrum; solid line is the logarithmic difference between the spectra. In all cases, the explosion has more high-frequency energy than the earthquakes. Top three figures correspond to the first three earthquakes in Figure 1, and bottom three to the last three.

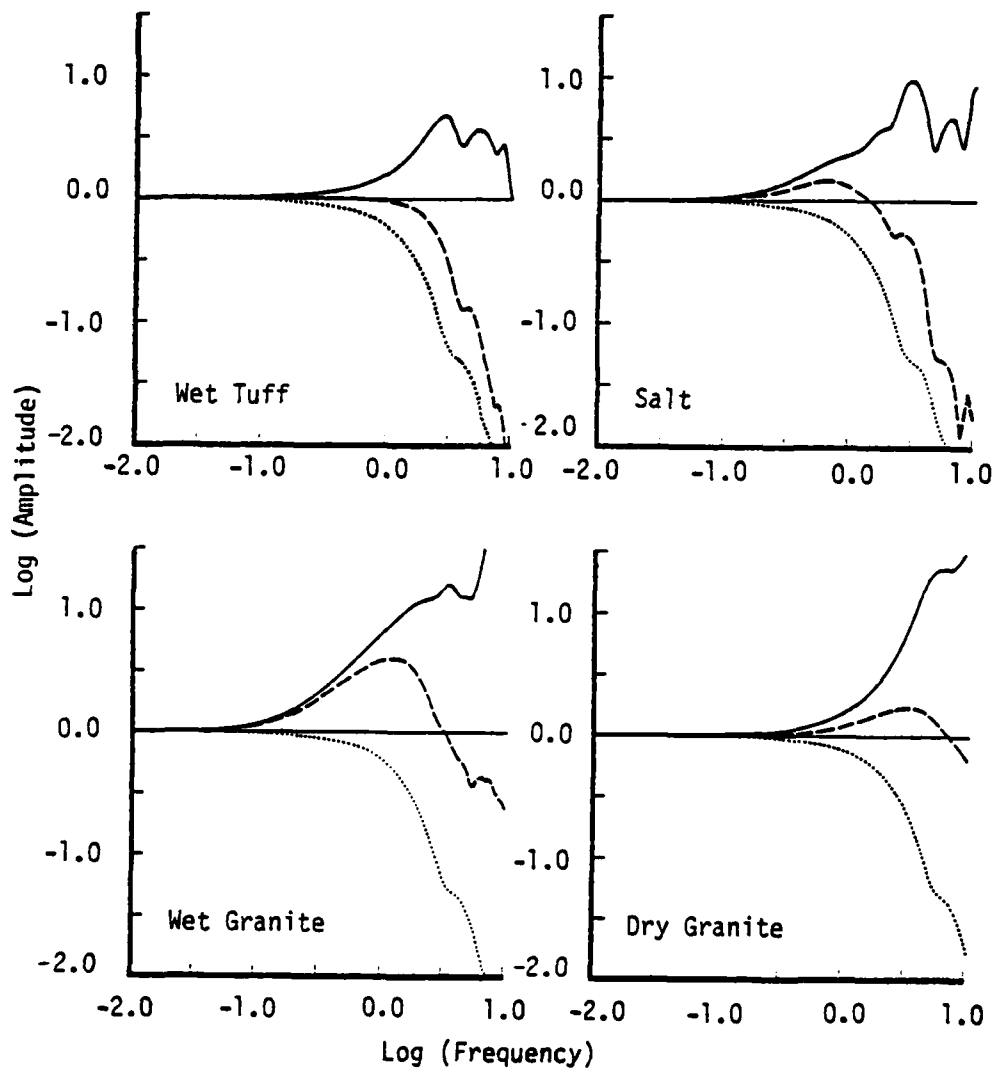


Figure 11. Spectral comparison of numerical explosion models at 100 KT with earthquake number 1 (approximately circular with 100 bar stress concentration). Again, all explosions have more high-frequency energy than the earthquake although some complexity is observed at very high-frequency.

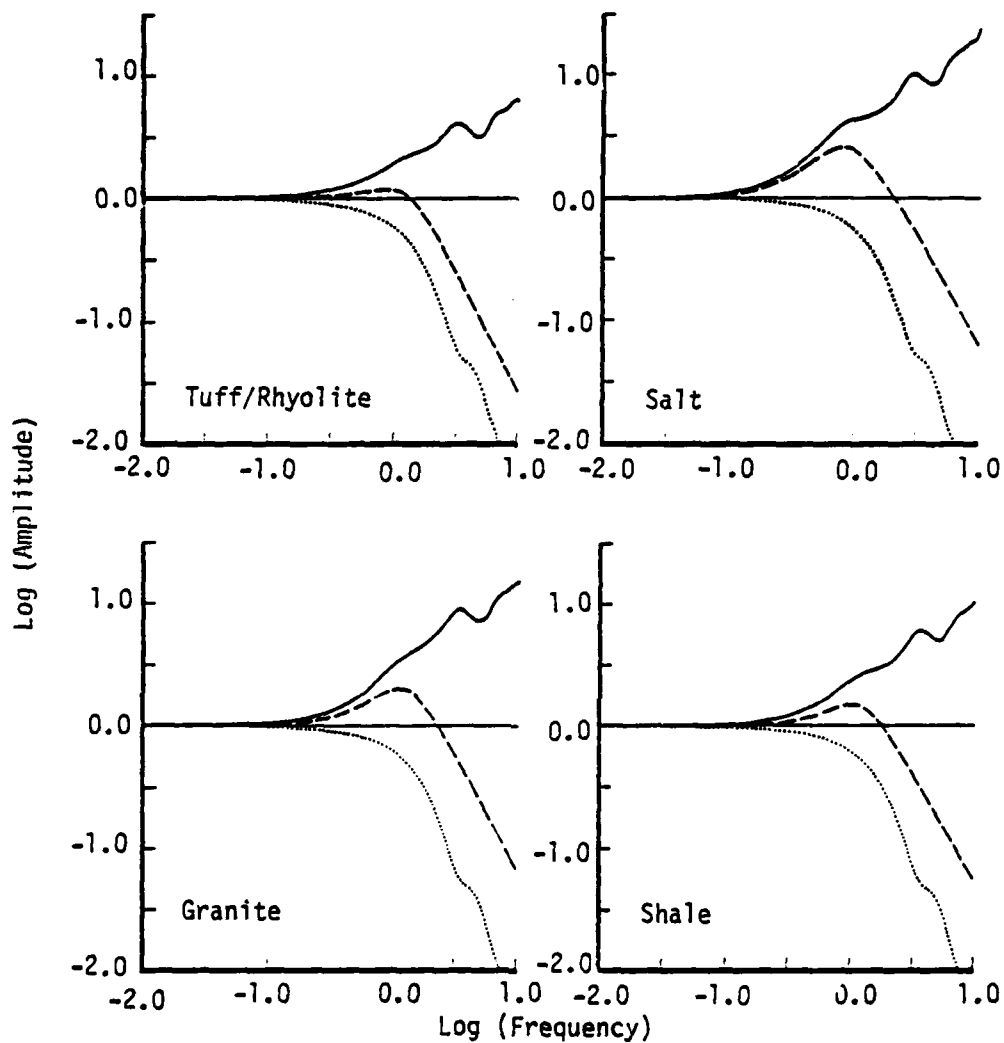


Figure 12. Spectral comparison of Mueller-Murphy explosion models at 100 KT with earthquake number 1.

earthquake-like at smaller yields. Figure 13 shows the Mueller-Murphy explosion source for tuff/rhyolite at a yield of 2.5 KT compared with earthquake number 3. On the basis of source spectrum, it would appear that very small explosions in low velocity materials may not be discriminated by VFM. However, at the shallow depth (165 meters) assumed for this source, interference with pP would allow discrimination.

The next set of figures, Figures 14 to 16, are synthetic variable frequency magnitude curves made by evaluating Equations 6.1a and 6.2a at two frequencies and scaling to a number of different amplitudes. Cube root scaling, as described earlier, was used for the numerical earthquake and explosion sources. The Mueller-Murphy sources were scaled with yield as described in Appendix A. The effect of radiation pattern was included by reducing m_b for earthquakes by using the c_b^x and c_b^q given before Equation 6.3.

The first pair of figures (Figure 14) are for a low frequency level $f_1 = .05$ Hz and high frequency levels of $f_2 = 1$ Hz and 2 Hz. The earthquake and explosion populations are separated on both plots, but the separation is quite small for $m_b < 4.5$ with $f_2 = 1$ Hz. Using $f_2 = 2$ Hz, the separation is much better. The populations are clearly separated for $m_b > 4.0$.

In practice, because the noise level increases at low frequencies, it is not possible to use frequencies much less than .5 Hz. Figure 15 shows synthetic VFM curves for $f_1 = .5$ Hz and $f_2 = 2, 3$ and 4 Hz. For small events, separation is almost as good as for $f_1 = .05$ Hz. For $f_2 = 4$ Hz, separation is quite clear even down to $m_b = 3.5$. For very large events, separation is not as good. This is because the low frequency level f_1 is moving above the corner frequency and seeing the high frequency complexity of the spectrum. Separation is especially good for explosions in higher velocity materials. Explosions in granite are much more clearly separated than explosions in tuff.

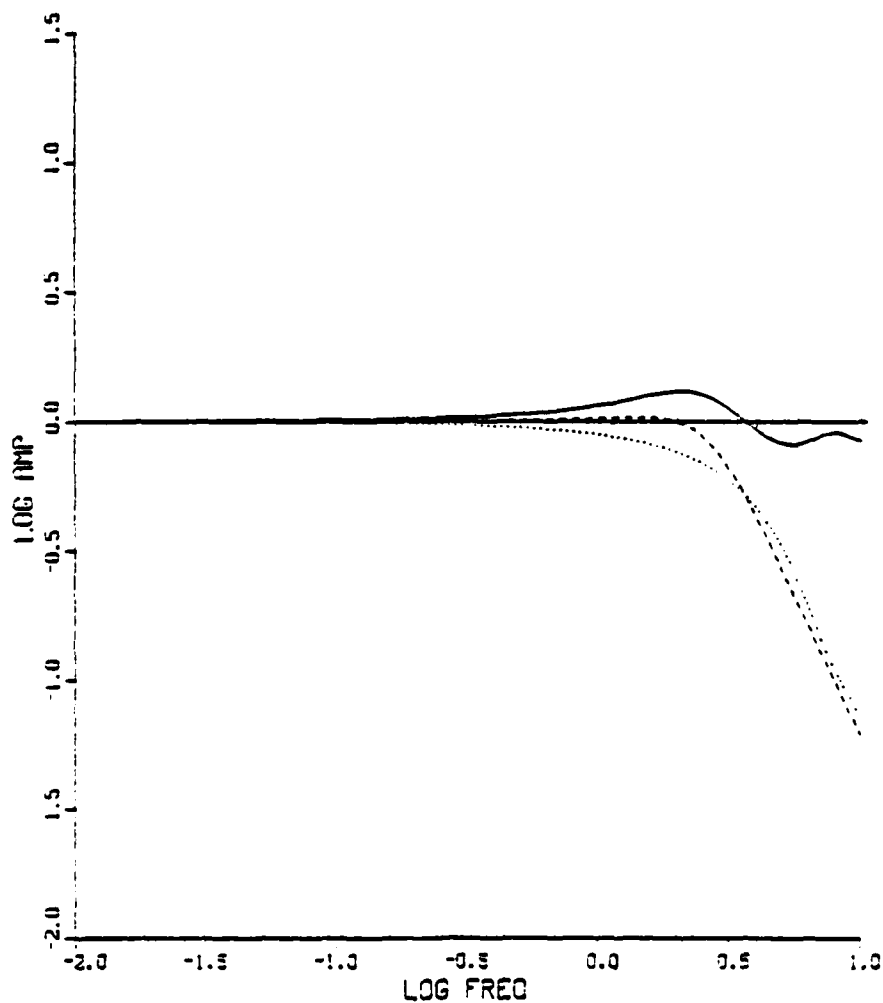


Figure 13. Spectral comparison of 2.5 KT Mueller-Murphy Tuff explosion with earthquake number 3. The only case in which explosions do not clearly have more high frequency energy than earthquakes is for the empirical model of small explosions in low velocity materials. Again, the dotted line is the earthquake, the dashed line is the explosion, and the solid line is the difference.

MARKS

Earthquakes —

1. Δ
2. \circ
3. $+$
4. \times
5. \diamond
6. ∇

Numerical Explosions - - -

- Wet tuff \blacksquare
- Dry Granite \ast
- Salt \blacklozenge
- Wet Granite \bullet

Empirical Explosions . . .

- Salt \boxplus
- Tuff/Rhyolite \blacksquare
- Granite \bullet
- Shale \square

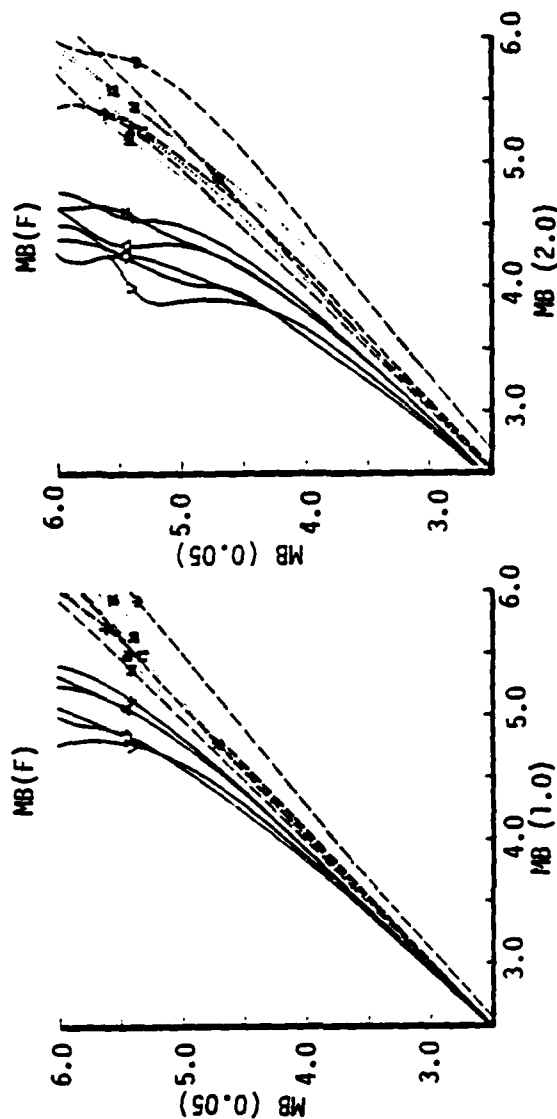


Figure 14. Synthetic variable frequency magnitude curves using $f_1 = 0.05$ Hz for the low frequency and $f_2 = 1.0$ Hz and 2.0 Hz for the high frequency. Solid lines are earthquakes marked at moment of 1017 NT-M. Dashed lines are numerical explosion sources; dotted are Mueller-Murphy explosion sources marked at 100 KT yield. The anomalously low amplitude mark is for dry granite. Separation of the earthquake and explosion populations is much better at 2 Hz.

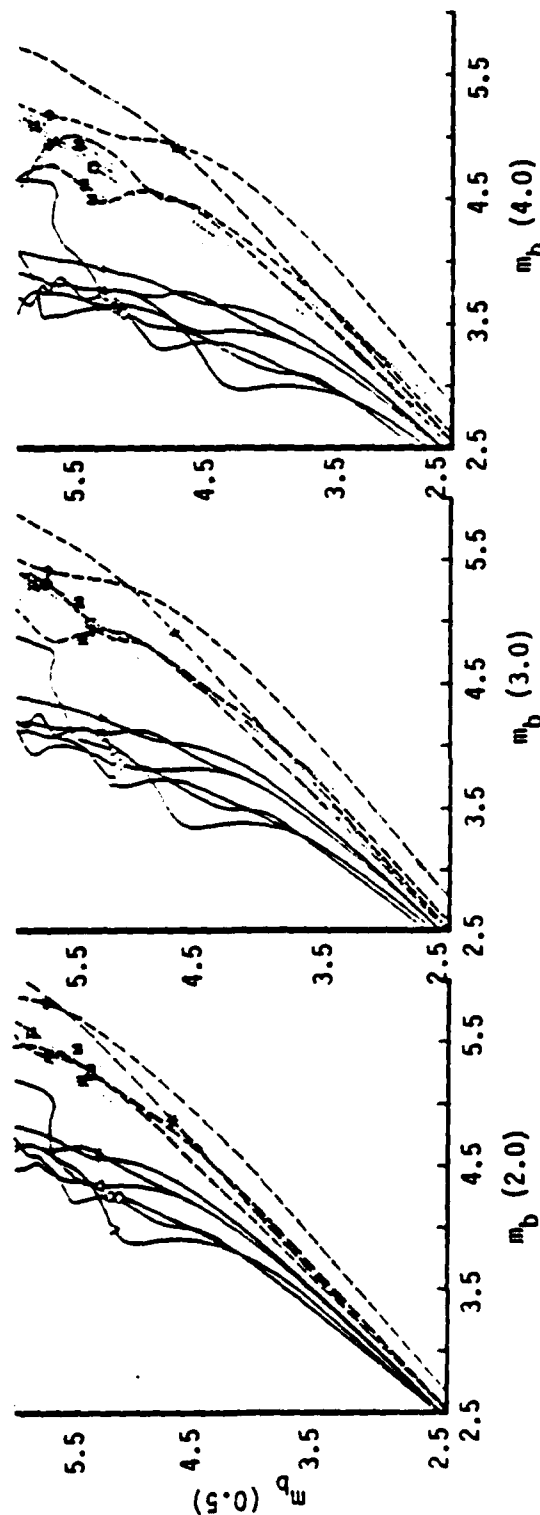


Figure 15. Synthetic Variable Frequency Magnitude curves for $f_1 = 0.5$ Hz, $f_2 = 2.0$, 3.0 , and 4.0 Hz. These are commonly used frequencies. The noise level increases rapidly below 0.5 Hz, and observations become difficult above 4.0 Hz.

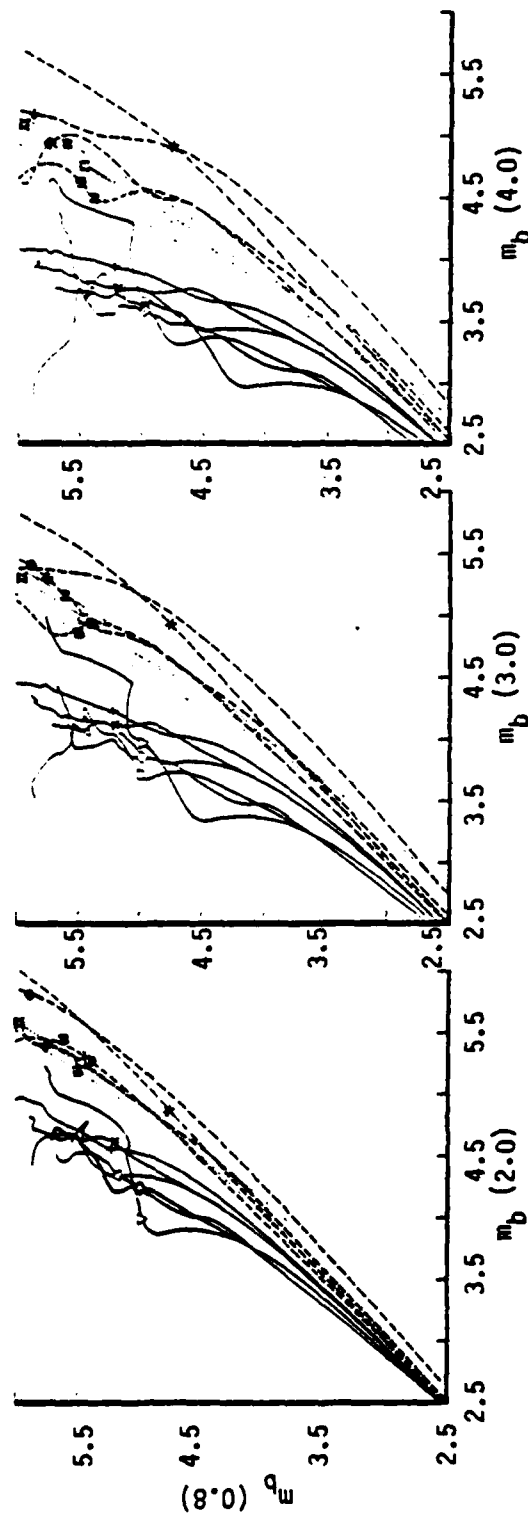


Figure 16. Synthetic Variable Frequency Magnitude curves for $f_1 = 0.8$ Hz, $f_2 = 2.0$, 3.0 and 4.0 Hz. The higher low frequency level is good for avoiding noise problems. Separation of the populations is still good, but becomes more difficult for larger events as the corner frequency moves below 0.8 Hz.

It could be advantageous to use a higher low-frequency level to avoid low-frequency noise. Figure 16 shows synthetic VFM curves for $f_1 = .8$ Hz and $f_2 = 2, 3$ and 4 Hz. The earthquake and explosion populations are still fairly well separated, but the region of clear separation is smaller than was the case with $f_1 = .5$ Hz. VFM measurements using $f_1 = .8$ Hz would be able to separate most events, but there is a greater chance of misidentification than there is using lower values of f_1 .

The synthetic VFM curves are quite insensitive to the assumptions we have made. A change in stress-drop of the earthquakes, for example, simply moves the earthquake curves along a 45 degree angle on the plots. Stress drops of 1 - 5 Kb are generally required to cause mixing of the earthquake and explosion populations. Explosions in granite only mix with very large, very high stress drop earthquakes. The numerical granite explosion models only mix with earthquakes with stress drops greater than 10 Kb and $m_b > 5.5$. Explosions in tuff do not discriminate as easily. There is some mixing with a stress drop of 250 bars at $m_b = 4.5$. Similarly, radiation pattern effects shift the earthquakes up or down along a 45 degree angle. The curves shown are for the average of the radiation pattern. At the maximum, there is a small amount of mixing with the Mueller-Murphy tuff source at low yields crossing into part of the earthquake population as the spectral comparison of Figure 13 showed. Earthquake Models 1, 3, and 4 mix with the explosions at much lower stress drop than Earthquake Models 2, 5, and 6.

We have used spectra evaluated exactly at the observation frequency for this comparison. In practice, any measurement is taken over a finite frequency window and will not be centered exactly at the desired frequency. VFM studies, however, use a very narrow band width; so this should be quite a good approximation.

Probably the most important approximation made here was the neglect of reflected body wave phases. As discussed earlier, these are expected to preferentially suppress $m_b(f_1)$, the low frequency magnitude, which will enhance event separation.

VII. TIME-DOMAIN SOURCE COMPARISON

In this section we make synthetic seismograms from our earthquake and explosion source functions and make measurements of m_b in the time-domain. While most of the essential source characteristics are contained in the preceding spectral comparisons, spectral estimates of m_b will not, in general, be equal to time-domain measurements of m_b . Time-domain amplitudes are measured using an instrument with a finite-frequency band width so the measured frequency will be shifted away from the dominant instrument frequency in the direction of increasing spectral amplitude.

Synthetic seismograms include the effects of source radiation pattern and interference of reflected and transmitted phases which were neglected or approximated earlier. The spectral comparisons in the last section used the root mean square spectra for the earthquakes, which lack some of the complexity of the position-dependent individual spectra. Time-domain comparisons include the phase information which was not used in the spectral comparisons.

To see how time-domain measurements compare with frequency-domain measurements, we made synthetic seismograms for a number of the earthquake and explosion sources. The seismograms were constructed using the modification of the method of Bache and Harkrider (1976) described in Appendix B.

The following parameters were used for all the earthquake synthetics. The earthquake is at a depth of 5 kilometers in a structure similar to the eastern U.S. structure S1 determined by Bache, Swanger and Shkoller, 1980, which is listed in Table 3. The receiver was located in a 4 km/sec half-space at a distance of 35 degrees (3900 km); so the takeoff angle from the source was 27 degrees. A t^* of .8 was used for attenuation. The fault was placed in 45 degree dip-slip orientation (strike = 0°, dip = 45°, rake = 90°) and observed at an azimuth of 90 degrees, near a maximum in the

Table 3

SOURCE REGION STRUCTURE FOR SYNTHETICS

<u>Layer</u>	<u>Depth (km)</u>	<u>(km/sec)^{α}</u>	<u>(km/sec)^{β}</u>	<u>(g/cm³)^{ρ}</u>
1	0.6	3.7	2.2	2.1
2	2.6	4.5	2.5	2.2
3	4.1	5.6	3.2	2.6
4	6.2	6.0	3.46	2.7
5	13.2	6.3	3.6	2.8
6	20.0	6.4	3.7	2.9
7	∞	6.6	3.8	3.0

radiation pattern. A few synthetics were also made at an azimuth of 270 degrees. Since we are interested primarily in differences in the source and source region, a geometric spreading factor of 1.2×10^{-4} was used in lieu of a mantle transfer function. A WWSSN short period instrument response was used. The maximum response of this instrument occurs at a period of .62 seconds.

We also made synthetic seismograms for the Mueller-Murphy explosion source functions in four different materials. The synthetic seismograms were made in the same manner as the earthquake seismograms using the method of Bache and Harkrider, except that the source region material constants were modified. The top two layers, to a depth of 2.6 km, were taken to have the same material properties as the explosion source material (as in Table 1). The Mueller-Murphy depth of $h = 122 W^{1/3}$, where h is in meters and W is in kilotons, was used for the explosion source depth.

Magnitude measurements were made to resemble, as much as possible, magnitude measurements from observed seismograms. For most cases, the amplitude used was the peak to peak amplitude from the first extremum to the second extremum. The period used was twice the time interval between these points. An exception to this method of measurement was made for some of the larger earthquakes. For these events the pulse duration was long enough that the amplitude became much larger after the first cycle. In these cases, the largest amplitude among the first few cycles was used. At the distance (35 degrees) used for the synthetics, the body wave magnitude m_b is defined by

$$m_b = \log_{10} \left(\frac{A}{GT} \right) + 3.4$$

where G is the gain of the instrument at period T , and A is the peak to peak amplitude in nanometers.

Measurements made from the synthetic seismograms are summarized in Tables 4 (earthquakes) and 5 (explosions). Shown on the tables are the moment of the event, m_b estimated from the

TABLE 4
MAGNITUDE ESTIMATES FROM SYNTHETIC EARTHQUAKE SEISMOGRAMS

Event #	$\log_{10}(M_0)$	$m_b(f)$	T/n	$m_b(T)$
1	17.10	5.11	1.04/1	5.76
	17.10	5.11	1.12/1b	5.73
	17.00	5.06	1.00/1	5.68
	16.40	4.66	.91/1	5.21
	15.80	4.15	.86/1	4.68
	14.50	2.87	.82/1	3.43
2	18.20	5.13	1.30/1	6.24
	17.38	5.00	1.13/1	5.78
	17.38	5.00	1.17/1b	5.77
	16.60	4.64	1.02/1	5.27
	16.00	4.24	.92/1	4.80
	15.00	3.38	.84/1	3.91
3	18.45	5.67	1.87/1	6.80
	18.45	5.67	1.62/1b	6.64
	17.70	5.44	1.24/1	6.32
	16.90	5.09	.94/1	5.70
	16.30	4.62	.87/1	5.18
	15.70	4.08	.83/1	4.62
4.	18.00	5.54	1.64/1	6.42
	18.00	5.54	1.12/1b	6.32
	17.50	5.30	1.38/1	6.12
	16.80	4.95	.99/1	5.56
	16.20	4.50	.89/1	5.06
	15.60	3.97	.84/1	4.52

TABLE 4 (continued)

MAGNITUDE ESTIMATES FROM SYNTHETIC EARTHQUAKE SEISMOGRAMS

Event #	$\log_{10}(M_0)$	$m_b(f)$	T/n	$m_b(T)$
5	18.10	5.23	1.28/5	6.52
	17.15	4.90	1.07/1	5.38
	17.15	4.90	1.16/1b	5.64
	16.70	4.68	1.21/1	5.20
	16.10	4.25	1.04/1	4.82
	15.40	3.70	.89/1	4.25
6	18.35	5.39	1.68/4	6.55
	18.35	5.39	1.13/4b	6.21
	17.80	4.84	1.78/1	6.09
	16.50	4.59	1.02/1	5.22
	15.90	4.16	.89/1	4.74
	15.30	3.65	.85/1	4.20

TABLE 5
MAGNITUDE ESTIMATES FROM SYNTHETIC EXPLOSION SEISMOGRAMS

Material	Yield	$\log_{10}(M_0)$	$m_b(f)$	T	$m_b(T)$
Salt	1	14.91	4.28	.71	4.07
	10	15.68	5.15	.73	5.09
	100	16.44	5.94	.77	6.07
	1000	17.21	6.58	.97	6.93
Tuff/Rhyolite	1	14.59	3.92	.70	3.76
	10	15.35	4.70	.72	4.79
	100	16.10	5.50	.82	5.74
	1000	16.87	6.24	1.06	6.53
Granite	1	14.87	3.88	.75	3.72
	10	15.63	4.72	.71	4.73
	100	16.39	5.65	.76	5.78
	1000	17.16	6.48	.89	6.75
Shale	1	14.64	3.81	.72	3.63
	10	15.40	4.62	.72	4.67
	100	16.16	5.49	.76	5.69
	1000	16.92	6.28	.97	6.59

frequency-domain measurements in the last section (at one Hertz), the period used for time-domain m_b , the number of the zero crossing used for the m_b measurement (b indicates measurement at 270 degrees azimuth), and, finally, the time-domain m_b measurement. In general, the time-domain m_b measurements are larger than the frequency-domain estimates. There are three reasons for this. First, the t^* of .8 may be lower than t^* of NTS. Bache et al. (1980) estimate a t^* of .8 to 1.05 for NTS explosions observed at different receiver stations. Hadley (1979) estimates t^* for NTS to lie in the range of 1.1 to 1.5 (Both t^* estimates were for a frequency of about one Hertz). Since our frequency-domain estimates are calibrated based on NTS shots in tuff, this increases both explosion and earthquake magnitudes by about a quarter of a magnitude compared to using a t^* of 1.0. Another possibility is that the mantle geometric spreading factor used here is too large. Second, the orientation of the faults puts the earthquake rays closer to a radiation pattern maximum than the average used in making frequency-domain estimates. This increases the amplitudes of the earthquakes by another quarter magnitude. Finally, there is an increase in amplitude caused by the shift in the dominant frequency away from the peak when the peak instrument response is above the corner frequency. Notice the increase in period as a function of the moment of the earthquake.

Figure 17 is a plot of time-domain m_b measurements for all of the earthquake and explosion sources listed in the tables. Explosion synthetics were made at 1 KT, 10 KT, 100 KT and 1000 KT. This figure may be compared with the frequency-domain figure (Figure 9) comparing m_b and M_s . The separation between the earthquake and explosion populations is still very clear; however, they appear to converge at small magnitudes. The reason for this is interference with pP. For the shallow 1 KT event in granite, interference reduces m_b by about 0.7; at 10 KT it reduces m_b by 0.2; at 100 KT it has little effect while at 1000 KT it increases m_b by about 0.3.

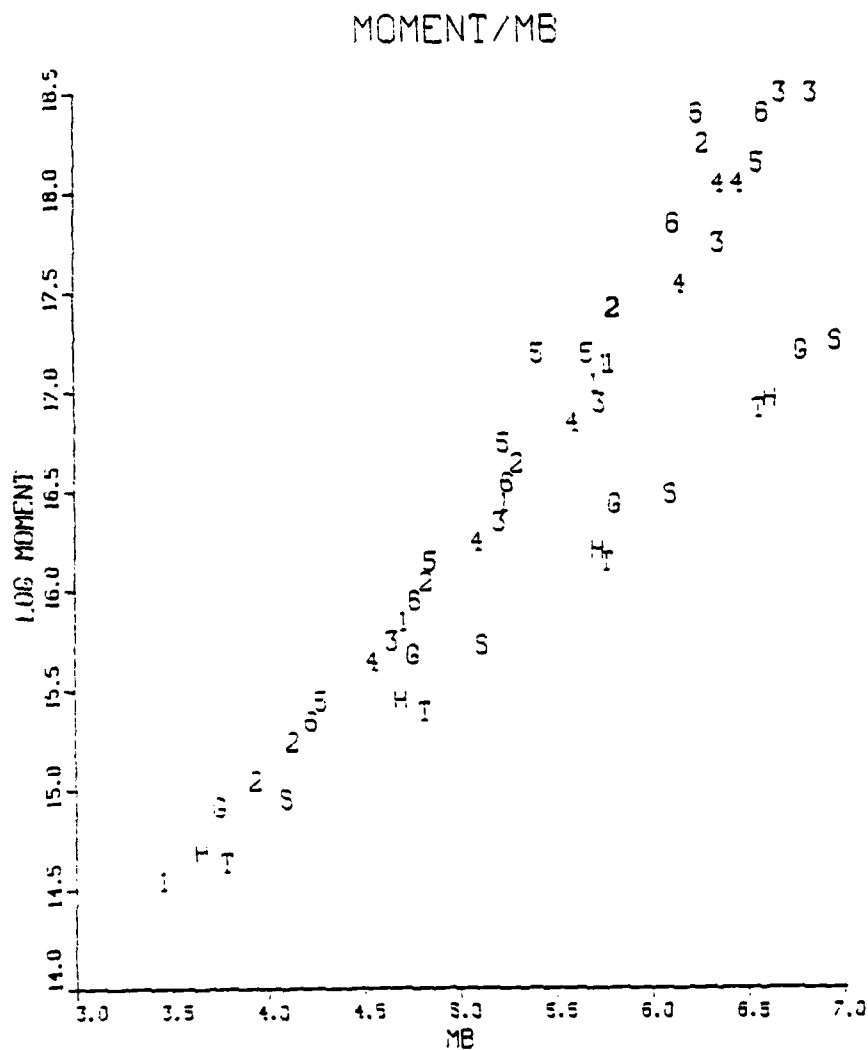


Figure 17. Time-domain m_b measurements from synthetic seismograms of the six earthquake sources scaled to different sizes and Mueller-Murphy explosion sources in salt (S), tuff (T), granite (G), and shale (H) at 1, 10, 100 and 1000 KT. Convergence at low magnitude is caused by increasing destructive interference of P and pP as explosions decrease in depth with decreasing yield.

VIII. RECOMMENDATIONS FOR FURTHER RESEARCH

In this report, we have tried to identify and quantify the important effects which allow or hinder discrimination. It is impossible, however, to examine every characteristic of earthquakes or explosions which might apply to this problem. We would like to mention some of the factors which we have not discussed in detail.

The extent of pP interference is quite important to both VFM and $m_b:M_s$ discrimination, especially for small explosions. Further work on how near surface nonlinearities such as cracking and spallation affect pP is needed. This is an active area of research, and nonlinear effects of pP are currently being modeled by two dimensional (cylindrically symmetric) nonlinear numerical calculations (Day, et al., 1981).

Our analysis of the frequency distribution of m_b and M_s was performed for a uniform half-space and then extended to a layer over a half-space. It would be possible to perform similar calculations for full layered half-space models. There would then be variations in seismic radiation due to the depth dependence of source region elastic properties and differences in the eigenfunctions of the layered half-space.

Von Seggern and Rivers (1979) performed an analysis similar to ours using a Gutenberg earth model. Their use of the root mean square amplitude of the distribution function rather than the peak of the distribution function (Figure 4) decreases the effect of source mechanism on earthquake/explosion separation from .35 to .22 magnitude units. They also find this number to be consistent in the upper 40 km except for a decrease to zero over a narrow range of depths near 5 km.

The best approach to the layered space problem would be to evaluate the relative excitation of surface waves for individual structures of interest. It would also be possible to perform the analysis for a restricted range of depths and/or orientations if the earthquakes in a given region are known to have preferred depths or orientations.

The six earthquake models in Figure 1 are based on plausible physical assumptions, and exhibit rupture histories and average stress drops which are consistent with what is known observationally about natural earthquakes. Nonetheless, they may not be fully representative of the entire range of phenomena relevant to the discrimination problem. One case of potential interest not considered here is that of a fault with a localized stress concentration many times greater than the average stress drop. Such a configuration has been inferred for the 1971 San Fernando Earthquake by several authors (e.g., Bache and Barker, 1978; Heaton and Helmberger, 1979). Some insight into this question is provided by Models 1 and 2. We find that Model 2 is easier to discriminate than Model 1 in spite of the fact that both have the same stress concentration at the center, indicating that an earthquake containing a stress concentration, but which propagates into a region of lower stress, will be easier to discriminate than failure of an isolated stress concentration which does not propagate further.

Our analysis of the VFM discriminant was based on spectral amplitudes. In practice, measurements are made in the time domain after narrow band filtering, and restricted to the first observed arrival at each frequency. There are also several different ways of smoothing the spectrum. It would be valuable to apply current VFM methods to a range of synthetic seismograms from earthquake and explosion models.

Another effect which can be important is explosion induced tectonic strain release. The effect of tectonic release on body and surface waves is discussed in detail using a linear approximation for explosions in complex prestress fields by Stevens (1982). In general, tectonic release adds energy to the seismic radiation and imposes a radiation pattern on the body and surface waves. Tectonic release can make discrimination more difficult, particularly if observations cover only a limited portion of the focal sphere. In some cases, tectonic release can aid discrimination by reducing surface wave amplitudes and increasing high frequency body wave

amplitudes. Nonlinear simulations of explosion induced tectonic release (e.g., Day, et al., 1981) are important in order to better determine the tectonic source and to understand how it interferes with and influences the explosion source.

Finally, we note that all of the analysis was performed for earthquakes and explosions in similar structures and may therefore not apply to the comparison of earthquakes in one area with explosions in another. Variations in attenuation and the frequency dependence of attenuation, as well as the amplitude response of a given structure, may strongly affect the discriminants. These variations can only be determined by a careful study of structure and attenuation in all areas of interest.

IX. DISCUSSION AND CONCLUSIONS

The theoretical results predict that both $m_b:M_s$ and variable frequency magnitude methods will successfully discriminate most earthquakes from underground explosions, but will be affected in very different ways by a number of important factors. While source spectral differences are important to both discriminants, differences in source mechanism (center of dilatation versus double-couple) and differences in source region elastic properties may dominate for small events using the $m_b:M_s$ discriminant. Free-surface reflected phases also play an important role at low magnitude, tending to inhibit $m_b:M_s$ discrimination and enhance VFM discrimination. Interference by pP is sufficient to cause the theoretical explosion population to begin to converge with the earthquake population on the $m_b:M_s$ plane at about $m_b = 4.5$. The latter conclusion, of course, depends on the assumption that the explosions are buried at normal containment depths and that pP is approximately elastic.

The average separation between the theoretical earthquake and explosion populations on the $m_b:M_s$ plane, excluding interference effects due to surface reflected phases, is given approximately by

$$M_s^q - M_s^x - (m_b^q - m_b^x) \approx .35 + .5 \log \left(\frac{\rho_q^3 \alpha_q^3}{\rho_x^3 \alpha_x^3} \right) + \text{spectral differences} ,$$

where x indicates explosion and q indicates earthquake, and ρ and α are source-region density and P-wave speed. The first term represents the effect of source mechanism, which is responsible for an average $m_b:M_s$ separation of .35 magnitude units between earthquake and explosion populations. For an earthquake and explosion of equal seismic moment, m_b of the explosion exceeds the average earthquake m_b by .45 units, while M_s of the explosion exceeds the average earthquake M_s by .1 unit. As shown in Figures 4 and 5, considerable scatter is introduced by variations in the source mechanism.

The second term represents the effect of source-region elastic properties. Source-region properties will usually increase the separation between earthquakes and explosions on the $m_b:M_s$ plane since explosions are shallower than most earthquakes, and so tend to be in lower-impedance materials. Small explosions in low-velocity, low density material are predicted to discriminate much more easily on $m_b:M_s$ than are small explosions in high-velocity, high-density material. This is true even though the explosion source spectrum is generally more earthquake-like (lower corner frequency, less peaked) in soft materials than in hard materials as can be seen in Figure 11, for example. In other words, in our theoretical results, the elastic wave-propagation effect of the source medium dominates over its competing effect on the explosion source spectrum for m_b less than about 5.5 (at one Hertz).

The third term, source spectral differences, accounts for most of the increasing $m_b:M_s$ separation predicted above $m_b \approx 4.5$ (see Figures 9 and 17). A consistent feature of the spectral magnitude estimates (Figure 8) and the synthetic seismogram magnitude estimates (Figure 16) is that Earthquake Model 3 falls nearest the explosion population followed closely by Models 4 and 1, while Models 2, 5, and 6 fall farther away. A crude explanation may be given for this behavior by considering three factors: rupture symmetry, rupture duration, and stress drop. The difficulty of discrimination is given approximately for each event by the (constant) product of $M_0 f_c^3$ where M_0 is the moment and f_c is the corner frequency. The corner frequency is (approximately) inversely proportional to the rupture duration; so a slow rupture velocity such as in Model 2 tends to enhance discrimination. In asymmetric faults such as Models 5 and 6, the fault area, and therefore the moment, is reduced when compared to a symmetric model such as Model 3, but the rupture duration is still determined by the longest dimension so that the corner frequency is approximately unchanged. Again, this enhances discrimination. Finally, the spontaneous rupture models (Models 1, 2, and 6) all extended into regions of lower prestress so that the average stress drops, and

therefore the moments, of these events are somewhat lower than the other models. This is, of course, a very rough explanation which combines subtle details of the amplitude and phase spectra of the source into the single gross feature "corner frequency," but it provides a partial physical explanation of the variability in discrimination potential between the earthquake models.

The important result here for discrimination studies is that the most difficult earthquakes to discriminate are those which are symmetric (approximately square or circular), have rapid rupture growth, and have uniformly high stress drop. This will be true both for $m_b:M_s$ and VFM discrimination. An interesting fact is that the complexity of Model 6 significantly enhances the predicted discrimination. Also, note that Model 2 is easier to discriminate than Model 1 in spite of the fact that they both have the same stress concentration at the center.

Variable frequency magnitude discrimination depends on spectral differences between earthquakes and explosions. The same spectral features of the earthquake models which affect $m_b:M_s$ also affect VFM. Models 2, 5, and 6 separate from explosions more easily than Models 3, 4, and 1 do. In most cases, we find that the theoretical explosion source function has more high-frequency energy than the earthquake source functions (scaled to 100 bars maximum stress drop); so the theoretical event populations are separated down to about $m_b = 3.5$. Explosions in saturated granite separate at even smaller magnitudes.

Explosions in high velocity materials such as granite should be more readily identified by VFM than explosions in lower velocity materials such as tuff, which is opposite to the low-magnitude behavior of $m_b:M_s$. For small, shallow explosions in low-velocity materials such as tuff, source spectral differences alone may be insufficient to achieve separation from the earthquake population (see Figure 13). Interference of pP can lower the low-frequency magnitude of shallow explosions by up to half a magnitude unit and should be adequate to permit most such events to

be discriminated. However, we have not performed a synthetic seismogram study of the VFM discriminant to confirm this conjecture. Conversely, over-burial of small explosions in soft rock may defeat the VFM discriminant. Of course, deep burial in soft rock should favor event identification by $m_b:M_s$.

To a surprising degree, we have found that the $m_b:M_s$ and VFM methods complement each other. The VFM method is predicted to be most effective for m_b ranging from about 3.5 to 5.5 whereas $m_b:M_s$ is predicted to be most effective above about $m_b = 4.5$ and to degenerate as magnitude decreases below $m_b \approx 4.5$, due to pP interference. Furthermore, at low magnitudes, $m_b:M_s$ is favored by soft explosion media, and VFM is favored by hard explosion media. As a third example, we find discrimination of small events by $m_b:M_s$ to be virtually uninfluenced by earthquake stress-drop whereas the VFM method, depending as it does primarily on source spectral difference, could conceivably be defeated by earthquakes with anomalously high stress-drops. Finally, $m_b:M_s$ fails for a few earthquake source orientations and depths for which surface wave excitation is anomalously low (notably very shallow, vertical dip-slip faults) while VFM is only slightly affected by source orientation. On the basis of this study, therefore, we conclude that simultaneous application of the $m_b:M_s$ and VFM methods will substantially increase the likelihood of correct event identification.

X. REFERENCES

- Aki, K. (1967), "Scaling Law of Seismic Spectrum," JGR, 72, pp. 1217-1231.
- Aki, K. (1972), "Scaling Law of Earthquake Source Time Function," Geophys. J., 31, pp. 3-25.
- Aki, K., M. Bouchon and P. Reasenber (1974), "Seismic Source Function for an Underground Nuclear Explosion," BSSA, 64, pp. 131-148.
- Aki, K. and P. G. Richards (1980), Quantitative Seismology, Theory and Methods, W. H. Freeman and Co., San Francisco.
- Archambeau, C. B. (1968), "General Theory of Elastodynamic Source Fields," Rev. Geophys., 15, pp. 241-288.
- Archambeau, C. B. (1972), "The Theory of Stress Wave Radiation From Explosions in Prestressed Media," Geophys. J. R. astr. Soc., 29, pp. 329-366.
- Archambeau, C. B., D. G. Harkrider and D. V. Helmberger (1974), "Studies of Multiple Seismic Events," California Institute of Technology Report to U.S. Arms Control and Disarmament Agency, ACDA/ST-220.
- Bache, T. C. and T. G. Barker (1978), "The San Fernando Earthquake — A Model Consistent With Near-Field and Far-Field Observations at Long and Short Periods," Systems, Science and Software Final Technical Report submitted to U. S. Geological Survey, SSS-R-78-3552, January.
- Bache, T. C., T. G. Barker, T. R. Blake, J. T. Cherry, D. G. Lambert, N. Rimer and J. M. Savino (1975), "An Explanation of the Relative Amplitudes of the Teleseismic Body Waves Generated by Explosions in Different Test Areas at NTS," Systems, Science and Software Final Report to the Defense Nuclear Agency, SSS-R-76-2746, October.
- Bache, T. C., J. T. Cherry, P. L. Coleman, S. M. Day, J. R. Murphy, N. Rimer and J. M. Savino (1980), "Seismological Discrimination and Yield Determination Research," Systems, Science and Software Final Report to the Advanced Research Projects Agency, SSS-R-80-4383, February.
- Bache, T. C., S. M. Day and J. M. Savino (1979), "Automated Magnitude Measures, Earthquake Source Modeling, VFM Discrimination Testing and Summary of Current Research," Systems, Science and Software Quarterly Technical Report to Advanced Research Projects Agency, SSS-R-79-3933, February.

- Bache, T. C. and D. G. Harkrider (1976), "The Body Waves Due to a General Seismic Source in a Layered Earth Model," BSSA, 66, pp. 1805-1819.
- Bache, T. C., D. G. Lambert and T. G. Barker (1980), "A Source Model for the March 28, 1975 Pocatello Valley Earthquake from Time-Domain Modeling of Teleseismic P-Waves," BSSA, 70, pp. 405-418.
- Bache, T. C., H. Swanger and B. Shkoller (1980), "Synthesis of Lg in Eastern United States Crustal Models with Frequency Independent Q," Systems, Science and Software Semiannual Technical Report to the Advanced Research Projects Agency, SSS-R-81-4668, September.
- Blandford, R. (1975), "A Source Theory for Complex Earthquakes," BSSA, 65, pp. 1385-1405.
- Bracewell, R. (1965), The Fourier Transform and Its Applications, McGraw-Hill, New York.
- Brune, J. N. (1970), "Tectonic Stress and the Spectra of Seismic Shear Waves from Earthquakes," JGR, 75, pp. 4997-5009.
- Burdick, L. J. and D. V. Helmberger (1979), "Time Functions Appropriate for Nuclear Explosions," BSSA, 69, pp. 957-973.
- Cerveny, and Ravindra (1971), Theory of Seismic Head Waves, University of Toronto Press.
- Cherry, J. T., N. Rimer and W. O. Wray (1975), "Seismic Coupling from a Nuclear Explosion: The Dependence of the Reduced Displacement Potential on the Nonlinear Behavior of the Near-Source Rock Environment," Systems, Science and Software Technical Report to Advanced Research Projects Agency, SSS-R-76-2742, September.
- Day, S. M. (1979), "Three-Dimensional Finite Difference Simulation of Fault Dynamics," Systems, Science and Software Final Report to NASA, SSS-R-80-4295, December.
- Day, S. M. (1982a), "Three-Dimensional Simulation of Fault Dynamics: Rectangular Faults with Fixed Rupture Velocity," BSSA, 72, No. 3, (in press).
- Day, S. M. (1982b), "Three-Dimensional Simulation of Spontaneous Rupture Propagation," BSSA, 72, No. 6, (in press).
- Day, S. M., T. C. Bache, T. G. Barker, J. T. Cherry (1978), "A Source Model for the 1975 Pocatello Valley Earthquake," Systems, Science and Software Scientific Report SSS-R-79-3893, December.

- Day, S. M., N. Rimer, and J. T. Cherry (1982), "Surface Waves From Underground Explosions With Spall: Analysis of Elastic and Nonlinear Source Models," (submitted to BSSA).
- Day, S. M., N. Rimer, J. T. Cherry, and J. L. Stevens (1981), "The Shagan River Story (The Effects of Spall and Prestress on m_b and M_s)," Proceedings of the VSC Research Conference, VELA Seismological Center Report, VSC-TR-82-1, P. 63-68.
- Douglas, A., J. A. Hudson and C. Blamey (1972), "A Quantitative Evaluation of Seismic Signals at Teleseismic Distances," Geophys J., 28, pp. 385-410.
- Douglas, A., J. A. Hudson and V. K. Kambhavi (1971), "The Relative Excitation of Seismic Surface and Body Waves by Point Sources," Geophys. J. R. astr. Soc., 23, pp. 451-460.
- Geller, R. J. (1976), "Scaling Relations for Earthquake Source Parameters and Magnitudes," BSSA, 66, pp. 1501-1523.
- Gilbert, F. (1973), "The Relative Efficiency of Earthquakes and Explosions in Exciting Surface Waves and Body Waves," Geophys. J. R. astr. Soc., 33, pp. 487-488.
- Hadley, D. M. (1979), "Seismic Source Functions and Attenuation from Local and Teleseismic Observations of the NTS Events JORUM and HANDLEY," Sierra Geophysics Quarterly Technical report to the Advanced Research Projects Agency, SGI-R-79-002, March.
- Hanks, T. C. (1974), "The Faulting Mechanism of the San Fernando Earthquake," JGR, 79, pp. 1215-1229.
- Hanks, T. C., and H. Kanamori (1979), "A Moment Magnitude Scale," JGR, 84, pp. 2348-2350.
- Hartzell, and J. N. Brune (1979), "The Horse Canyon Earthquake of August 2, 1975 -- Two-Stage Stress-Release Process in a Strike-Slip Earthquake," BSSA, 69, pp. 1161-1173.
- Haskell, N. A (1964), "Total Energy and Energy Spectral Density of Elastic Wave Radiation from Propagating Faults," BSSA, 54, pp. 1811-1841.
- Haskell, N. A. (1966), "Total Energy and Energy Spectral Density of Elastic Wave Radiation from Propagating Faults, II: A Statistical Fault Model," BSSA, 56, pp. 125-140.
- Heaton, T. H. and P. V. Helmberger (1979), "Generalized Ray Models of the San Fernando Earthquake," BSSA, 69, pp. 1311-1341.
- Helmberger, D. V. and D. G. Harkrider (1972), "Seismic Source Descriptions of Underground Explosions and a Depth Discriminate," Geophys. J. R. astr. soc., 31, pp. 45-66.

- Kanamori, H. and D. L. Anderson (1975), "Theoretical Basis of Some Empirical Relations in Seismology," BSSA, 65, pp. 1073-1095.
- Kostrov, (1968), "The Inverse Problem of the Theory of Earthquake Foci," Izv. Earth Physics, 9, pp. 18-29.
- Marshall, P. E. and P. W. Basham (1972), "Discrimination Between Earthquakes and Underground explosions Employing an Improved M_s Scale," Geophys. J. R. astr. Soc., 28, pp. 431-458.
- Masse, R. P. (1981), "A Review of Seismic Source Models for Underground Nuclear Explosions," BSSA, 71, pp. 1249-1268.
- Mueller, R. A. and J. R. Murphy (1971), "Seismic Characteristics of Underground Nuclear Detonations," BSSA, 61, pp. 1675-1692.
- Murphy, J. R. (1977a), "Seismic Source Functions and Magnitude Determinations for Underground Nuclear Detonations," BSSA, 67, pp. 135-158.
- Murphy, J. R. (1977b), "Seismic Coupling and Magnitude/Yield Relations for Underground Nuclear Detonations in Salt, Granite, Tuff/Rhyolite and Shale Emplacement Media," Computer Sciences Corporation Technical Report CSC-TR-77-0004, December.
- Murphy, J. R. and Mueller, R. A. (1971), "Seismic Characteristics of Underground Nuclear Detonations, II," BSSA, 61, pp. 1693-1704.
- Richter, C. F. (1958), Elementary Seismology, W. H. Freeman and Co., San Francisco.
- Savino, J. M., C. B. Archambeau, and J. F. Masso (1980), "Discrimination Results From a 10 Station Network," Systems, Science and Software Technical Report to Advanced Research Projects Agency, SSS-R-80-4566, July.
- Stevens, J. L. (1980), "Seismic Radiation From the Sudden Creation of a Spherical Cavity in an Arbitrarily Prestressed Elastic Medium," Geophys. J. R. astr. Soc., 61, pp. 303-328.
- Stevens, J. L. (1982), "A Model for Tectonic Strain Release From Explosions in Complex Prestress Fields Applied to Anomalous Seismic Waves From NTS and Eastern Kazakh Explosions," Systems, Science and Software Technical Report submitted to VELA Seismological Center, SSS-R-82-5358, January.
- Tsai, Y. and K. Aki (1971), "Amplitude Spectra of Surface Waves from Small Earthquakes and Underground Nuclear Explosions," JGR, 76, pp. 3940-3952.
- Von Seggern, D. and R. Blandford (1972), "Source Time Functions and Spectra for Underground Nuclear Explosions," Geophys. J. R. astr. Soc., 31, pp. 83-97.

Von Seggern, D. H. and D. W. Rivers (1979), "Seismic Discrimination of Earthquakes and Explosions with Application to the Southwestern United States," Seismic Data Analysis Center Report, SDAC-TR-77-10, March.

APPENDIX A

MUELLER-MURPHY EXPLOSION SOURCE FUNCTION
AND SCALING LAWS

APPENDIX A

MUELLER-MURPHY EXPLOSION SOURCE FUNCTION AND SCALING LAWS

The Mueller-Murphy empirical scaling laws give the source time function for explosions in different materials as a function of yield and depth (Mueller and Murphy, 1971; Murphy and Mueller, 1971; Murphy 1977a, 1977b). As a general rule, larger explosions will be more deeply buried (for containment). We expect depth to scale approximately with the cube root of yield; that is,

$$h \approx h_0 W^{1/3} ,$$

where h is the explosion depth, W is the yield and h_0 is an empirical constant. For most materials $h_0 \approx 122 \text{ m/KT}^{1/3}$. The source is taken to be a pressure pulse of the form

$$P(t) = (P_0 e^{-\gamma t} + P_2) H(t) ,$$

applied at the elastic radius R . The values of P_0 , P_2 , γ and R are given by

$$P_1 = P_{10} h/h_0$$

$$R = R_0 (h_0/h)^{1/n} W^{1/3}$$

$$P_2 = P_{20} (h_0/h)^{1/3} (R_0/R)^3 W^{.87}$$

$$\gamma = \gamma_0 R_0/R$$

$$P_0 = P_1 - P_2$$

The empirical constants are given in Table A for yield in kilotons (Murphy, 1977b). The reduced velocity potential ($\dot{\psi}$) is then given by:

$$\dot{\psi}(\omega) = \left(\frac{P_0}{\gamma + i\omega} + \frac{P_2}{i\omega} \right) \frac{i\omega R \alpha^2}{4\mu} \frac{e^{i\omega R/\alpha}}{\omega_0^2 + i\omega_0\omega - \frac{\lambda + 2\mu}{4\mu} \omega^2}$$

where α is the P-wave velocity, λ and μ are the elastic constants and $\omega_0 = \alpha/R$.

The far-field displacement (for any RVP) is given at a distance r by

$$u(r, \omega) = \frac{\dot{\psi}(\omega) e^{-i\frac{\omega r}{\alpha}}}{\alpha r}$$

The long period limit ψ_∞ is given by

$$\begin{aligned} \psi_\infty &= \frac{P_2 R^3}{4\mu} \\ &= \frac{P_{20} R_0^3}{4\mu} W^{-.76} \quad \text{for} \quad h = h_0 W^{1/3} \end{aligned}$$

For all materials except salt, if $h = h_0 W^{1/3}$, then P_1 scales as $W^{1/3}$ while P_2 and R , which are affected by overburden pressure, vary approximately as $W^{-.20}$.

TABLE A
MUELLER/MURPHY EMPIRICAL CONSTANTS

Constants	Tuff/Rhyolite	Granite	Salt	Shale	
h_0	122	122	122	122	meters
R_0	202	321	478	265	meters
r_0	26	34	31	42	sec ⁻¹
P_{10}	36	46	55	42	bars
P_{20}	50	24	8	25	bars
n	2.4	2.4	1.87	2.4	

APPENDIX B

EQUIVALENT JUMP VECTORS FROM UPGOING AND DOWNGOING WAVES

APPENDIX B

EQUIVALENT JUMP VECTORS FROM UPGOING AND DOWNGOING WAVES

We want to make synthetic seismograms using the method of Bache and Harkrider (1976) when the source is described in terms of upgoing and downgoing waves. Bache and Harkrider's method starts with a multipolar expansion for the source, derives equivalent jump vectors and uses a saddle point approximation for the far field displacement.

In general, a source may be described in cylindrical coordinates by three potentials:

$$\rho(r, \theta, z, \omega) = \sum_{m=0}^{\infty} \int_0^{\infty} S_{1m}^+(\omega, k) e^{-ikr_a|z-h|} J_m(kr) dk$$

$$\psi(r, \theta, z, \omega) = \sum_{m=0}^{\infty} \int_0^{\infty} S_{2m}^+(\omega, k) e^{-ikr_b|z-h|} J_m(kr) dk$$

$$\chi(r, \theta, z, \omega) = \sum_{m=0}^{\infty} \int_0^{\infty} S_{3m}^+(\omega, k) e^{-ikr_b|z-h|} J_m(kr) dk$$

where \pm correspond to $z \gtrless h$, with h the source depth. The potential χ corresponds to SH waves and is decoupled from the other potentials. Using the saddle point approximation as in the Bache and Harkrider paper, the far-field displacements are found to be

$$U_p = \sum_m S_{1m}^+ i^m r_a k_a \frac{e^{-ik_a R}}{R}$$

$$U_{SV} = - \sum_m S_{2m}^+ i^{m+1} r_b k_b \frac{e^{-ik_b R}}{R}$$

$$U_{SH} = - \sum_m S_{3m}^+ i^m r_b k \frac{e^{-ik_b R}}{R}$$

we have used the definition

$$r_v = \left(\frac{c^2}{v^2} - 1 \right)^{1/2}$$

where c is the phase velocity. In the far-field approximation, $k = \omega/c$ corresponds to a particular ray for which $c = \frac{v}{\sin \theta}$ where θ is the takeoff angle of the ray and v is the appropriate velocity α or β . The equation for U_{SV} (in Equation 33 of Bache and Harkrider) is in error and should be multiplied by $-i$.

We compare these equations with the far-field displacements for the earthquake source:

$$U_p = \frac{1}{4\pi\rho\alpha^3} \frac{e^{-ik_\alpha R}}{R} R_p(\theta, \phi) \Omega_p(\theta, \phi, \omega)$$

$$U_{SV} = \frac{1}{4\pi\rho\beta^3} \frac{e^{-ik_\beta R}}{R} R_{S\theta}(\theta, \phi) \Omega_S(\theta, \phi, \omega)$$

$$U_{SH} = \frac{1}{4\pi\rho\beta^3} \frac{e^{-ik_\beta R}}{R} R_{S\phi}(\theta, \phi) \Omega_S(\theta, \phi, \omega)$$

Here R_p , $R_{S\theta}$, $R_{S\phi}$ are radiation pattern coefficients (see Appendix D) which are independent of frequency, and Ω_p and Ω_S are source spectra obtained by integrating the slip velocity over the fault plane (see Appendix C). Comparing these two sets of equations, we find

$$\sum i^m S_{1m}^+ = \frac{R_p(\theta, \phi) \Omega_p(\theta, \phi, \omega)}{4\pi\rho\alpha^3 r_\alpha k_\alpha}$$

$$\sum i^m S_{2m}^+ = \frac{i R_{S\theta}(\theta, \phi) \Omega_S(\theta, \phi, \omega)}{4\pi\rho\beta^3 k_\beta r_\beta}$$

$$\sum i^m S_{3m}^+ = \frac{-R_{S\phi}(\theta, \phi) \Omega_S(\theta, \phi, \omega)}{4\pi\rho\beta^3 k_\beta r_\beta}$$

where θ , ϕ and k all correspond to the appropriate directions for upgoing and downgoing waves.

From this result we can derive equivalent jump vectors for the earthquake source. Using the notation of Bache and Harkrider and the results of Harkrider (1964),

$$\delta U_m = k^2 [(S_{1m}^+ - S_{1m}^-) - ikr_\beta (S_{2m}^+ + S_{2m}^-)]$$

$$\delta W_m = ik[-ikr_\alpha (S_{1m}^+ + S_{1m}^-) + k^2 (S_{2m}^+ - S_{2m}^-)]$$

$$\delta Z_m = k^2 c^2 \rho [(\gamma - 1)(S_{1m}^+ - S_{1m}^-) - ikr_\beta \gamma (S_{2m}^+ + S_{2m}^-)]$$

$$\delta X_m = k^2 c^2 \rho [-\gamma r_\alpha (S_{1m}^+ + S_{1m}^-) - ik(\gamma - 1)(S_{2m}^+ - S_{2m}^-)]$$

where

$$\gamma = 2 \left(\frac{\beta}{c}\right)^2 .$$

For the tangential waves

$$\delta V_m = ik^2 (S_{3m}^+ - S_{3m}^-)$$

$$\delta Y_m = -ik^2 \mu r_\beta (S_{3m}^+ + S_{3m}^-)$$

The equivalent jump vectors in terms of upgoing and downgoing waves are defined by

$$\delta \bar{U} = \sum_m i^m \delta U_m$$

with similar definitions for the other jump vectors. These may be evaluated directly from the upgoing waves and used in Equation 28 of Bache and Harkrider. This removes the m index on all remaining

equations with the final result for the far-field displacement from an earthquake in a layered medium (equivalent to their Equation 33)

$$U_P = \frac{-r_a}{k_a} \Delta_n \frac{e^{-ik_a R}}{R}$$

$$U_{SV} = \frac{-2r_b}{k_b} \omega_n \frac{e^{-ik_b R}}{R}$$

$$U_{SH} = -r_b \epsilon_n \frac{e^{-ik_b R}}{R}$$

APPENDIX C

INTERPOLATION METHOD

APPENDIX C

INTERPOLATION METHOD

The evaluation of the source time function from the finite difference calculations requires the evaluation of surface integrals over the failure surface which can be reduced to a three-dimensional Fourier transform (Day et al., 1978). The integrals have the form

$$\Omega_p(\theta, \phi, \omega) = \mu \int_{-\infty}^{\infty} \int_{-\infty}^{\infty} \int_{-\infty}^{\infty} dx_0 dy_0 dt \dot{s}(x_0, y_0, t) e^{i(K_x x_0 + K_y y_0 - \omega t)} \left| \begin{array}{l} K_x = \frac{\omega}{a} \sin \theta \cos \phi \\ K_y = \frac{\omega}{a} \sin \theta \sin \phi \end{array} \right.$$

$$\Omega_s(\theta, \phi, \omega) = \mu \int_{-\infty}^{\infty} \int_{-\infty}^{\infty} \int_{-\infty}^{\infty} dx_0 dy_0 dt \dot{s}(x_0, y_0, t) e^{i(K_x x_0 + K_y y_0 - \omega t)} \left| \begin{array}{l} K_x = \frac{\omega}{b} \sin \theta \cos \phi \\ K_y = \frac{\omega}{b} \sin \theta \sin \phi \end{array} \right.$$

where \dot{s} is the slip velocity which is known at evenly spaced intervals of x_0 , y_0 , and t . The x and y coordinates are Cartesian coordinates in the fault plane. The angles θ and ϕ are spherical coordinates of the observer, with θ measured from the fault normal, and ϕ measured in the fault plane.

The results of the surface integration give Ω_p , Ω_s at evenly spaced intervals of K_x , K_y when an FFT is used. For the computation of a particular ray leaving at an angle θ , ϕ , we will therefore need to interpolate in the K_x , K_y plane to find the spectrum at the appropriate ray parameters for each frequency.

The method of interpolation is described by Bracewell (1965) and consists of convolution of the function known at evenly spaced points with the two-dimensional sinc function

$$s(K_x, K_y) = \frac{\tau_x \tau_y}{\pi^2} \frac{\sin \frac{\pi K_x \tau_x}{2}}{K_x} \frac{\sin \frac{\pi K_y \tau_y}{2}}{K_y}$$

The interpolated values will be exact as long as the transformed function is zero outside of the interval

$$-\frac{\tau_x}{2} < x < \frac{\tau_x}{2} \quad , \quad -\frac{\tau_y}{2} < y < \frac{\tau_y}{2}$$

where x, y are the transform variables corresponding to K_x, K_y . We can write the function at discrete points in the form

$$F(K_x, K_y) = \sum_{n=-\infty}^{\infty} \sum_{m=-\infty}^{\infty} f(n\tau_x, m\tau_y) \delta(K_x - n\tau_x) \delta(K_y - m\tau_y) \quad .$$

Convolution with the sinc function gives

$$f(K_x, K_y) = \frac{\tau_x \tau_y}{\pi^2} \iint dx' dy' \sum_{m,n} f(n\tau_x, m\tau_y) \delta(x' - n\tau_x) \delta(y' - m\tau_y) \\ \times \frac{\sin[\frac{\pi}{\tau_x} (K_x - x')] \sin[\frac{\pi}{\tau_y} (K_y - y')]}{(K_x - x') (K_y - y')} \quad .$$

If $K_x = q\tau_x$ and $K_y = p\tau_y$, then, using

$$\sin(\pi q - n\pi) = (-1)^n \sin \pi q \quad ,$$

we have

$$f(K_x, K_y) = \frac{\sin \pi q \sin \pi p}{\pi^2} \sum_{n,m} (-1)^{n+m} \frac{f(n\tau_x, m\tau_y)}{(q-n)(p-m)} \quad .$$

If either p or q is an integer, the integral becomes one-dimensional. If $K_x = n\tau_x$, then

$$f(K_x, K_y) = \frac{\sin \pi p}{\pi} \sum_m (-1)^m \frac{f(n\tau_x, m\tau_y)}{p-m} \quad .$$

The one-dimensional interpolator is also very useful for interpolating the frequency spectrum. If $\omega = p\tau$, then

$$f(\omega) = \frac{\sin \pi p}{\pi} \sum_m (-1)^m \frac{f(m\tau)}{p-m} \quad .$$

This, again, will be exact as long as the transformed function exists only in the time interval

$$-\frac{1}{2\tau} < t < \frac{1}{2\tau} \quad .$$

APPENDIX D

UPGOING AND DOWNGOING WAVES FOR ARBITRARY FAULT ORIENTATION

APPENDIX D

UPGOING AND DOWNGOING WAVES FOR ARBITRARY FAULT ORIENTATION

As described in the previous appendix, a surface integral can be performed to give the outgoing waves in any direction. We are interested in the waves which correspond to upgoing and downgoing waves in a half-space. The source and half-space coordinate systems are shown in Figure 18. We need to determine the angles θ and ϕ in the fault coordinate system for both the upgoing (-) and downgoing (+) waves for an arbitrary fault orientation. These angles will then be used to find the appropriate values of K_x and K_y as described in the last appendix and to include the radiation pattern.

From Aki and Richards, the slip and normal vectors are given in terms of the strike ϕ_s , dip δ , and rake λ in the half space coordinate system by

$$\begin{aligned} \hat{s} &= (\cos\lambda \cos\phi_s + \cos\delta \sin\lambda \sin\phi_s, \\ &\quad \cos\lambda \sin\phi_s - \cos\delta \sin\lambda \cos\phi_s, -\sin\lambda \sin\delta) \end{aligned} \quad (D.1)$$

$$\hat{n} = (-\sin\delta \sin\phi_s, \sin\delta \cos\phi_s, -\cos\delta)$$

The vectors \underline{k}^+ and \underline{k}^- are defined by the takeoff angle and azimuth of the observation point

$$\begin{aligned} \underline{k}^+ &= (\sin\theta_t \cos\phi_t, \sin\theta_t \sin\phi_t, \cos\theta_t) \\ \underline{k}^- &= (\sin\theta_t \cos\phi_t, \sin\theta_t \sin\phi_t, -\cos\theta_t) \end{aligned} \quad (D.2)$$

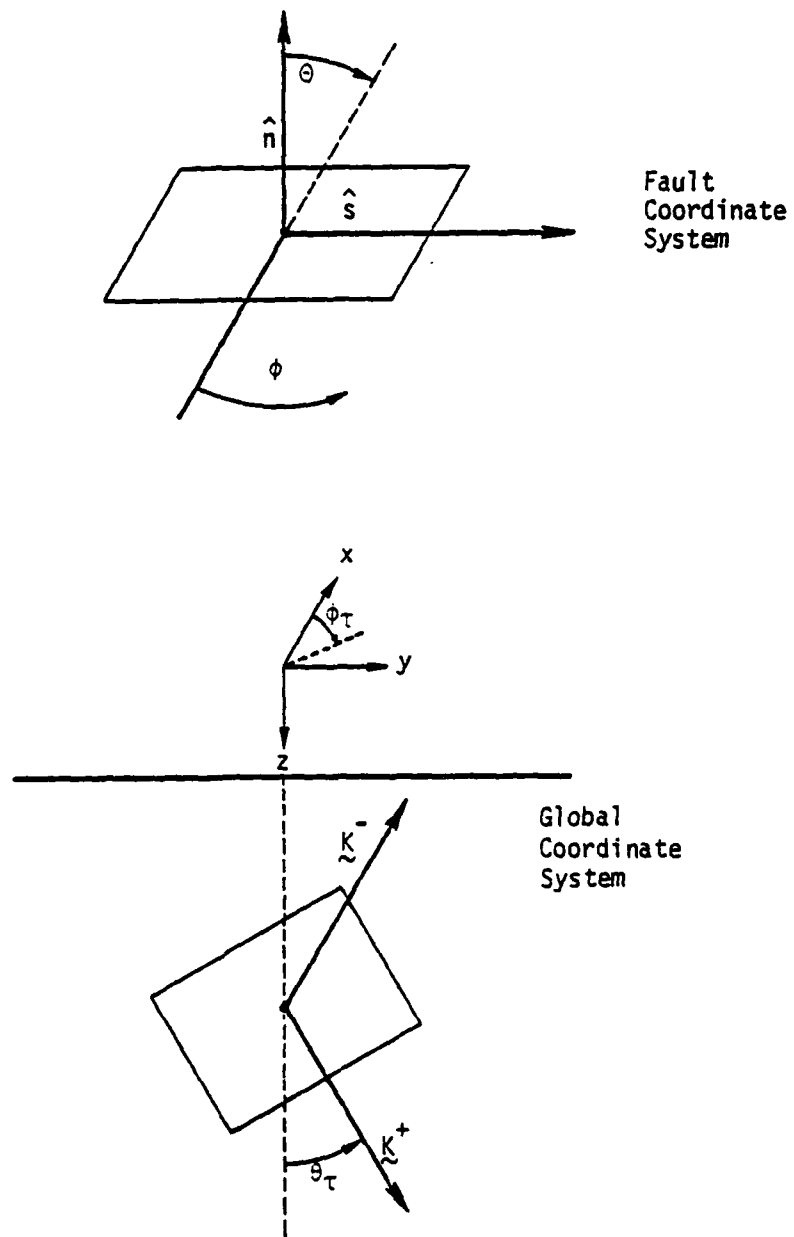


Figure 18. Fault and global coordinates used for synthetic seismograms.

From these we need the angles in the earthquake frame θ^{\pm} , ϕ^{\pm} .

A unit vector in the earthquake coordinate system is given by

$$\hat{e} = (\sin\theta \cos\phi, \sin\theta \sin\phi, \cos\theta)$$

with

$$\hat{s} = (0, 1, 0), \quad \hat{n} = (0, 0, 1) \text{ and } \hat{s} \times \hat{n} = (1, 0, 0) ;$$

so, using \hat{K} as the unit vector,

$$\hat{n} \cdot \underline{\hat{K}}^{\pm} = \pm \cos\theta^{\pm}$$

$$\hat{s} \cdot \underline{\hat{K}}^{\pm} = \sin\theta^{\pm} \sin\phi^{\pm}$$

$$(\hat{s} \times \hat{n}) \cdot \underline{\hat{K}}^{\pm} = \sin\theta^{\pm} \cos\phi^{\pm} .$$

Using Equations D.1 and D.2 to compute \hat{n} , \hat{s} , $\underline{\hat{K}}^+$ and $\underline{\hat{K}}^-$ in the half space frame gives the angles θ^{\pm} , ϕ^{\pm} in the earthquake frame. The values of K_x , K_y can now be found:

For P-waves

$$K_x^+ = \frac{\omega}{\alpha} \sin\theta^+ \cos\phi^+$$

$$K_y^+ = \frac{\omega}{\alpha} \sin\theta^+ \sin\phi^+$$

For S-waves

$$K_x^+ = \frac{\omega}{\beta} \sin\theta^+ \cos\phi^+$$

$$K_y^+ = \frac{\omega}{\beta} \sin\theta^+ \sin\phi^+ .$$

For a particular problem, the same K_x^+ , K_y^+ is used for both P-waves and S-waves. θ_t , ϕ_t correspond to the takeoff angle of the wave of interest.

The radiation pattern factors in the earthquake coordinate system are

$$R_p = \sin 2\theta \sin \phi$$

$$R_{S\theta} = \cos 2\theta \sin \phi$$

$$R_{S\phi} = \cos \theta \cos \phi \quad .$$